



Paleoenvironmental redox evolution of Ediacaran-Cambrian restricted seas in the core of West Gondwana: Insights from trace-metal geochemistry and stratigraphy of the Bambuí Group, east Brazil

Cristian Guacaneme^{a,*}, Sergio Caetano-Filho^a, Gustavo M. Paula-Santos^b, Marly Babinski^a, Paula L. Fraga-Ferreira^c, Carolina Bedoya-Rueda^a, Matheus Kuchenbecker^{d,e}, Humberto L.S. Reis^f, Ricardo I.F. Trindade^g

^a Universidade de São Paulo, Instituto de Geociências, Rua Do Lago 562, São Paulo, SP, ZIP Code 05508-080, Brazil

^b University of Bremen, Faculty of Geosciences and MARUM-Center for Marine Environmental Sciences, Leobener Strasse 8, 28359, Bremen, Germany

^c GEOMAR Helmholtz Centre for Ocean Research, Paleogeography Department, Wischhofstraße 1-3, Kiel, 24148, Germany

^d Universidade Federal Dos Vales Do Jequitinhonha e Mucuri, Instituto de Ciência e Tecnologia, Centro de Estudos Em Geociências, Laboratório de Estudos Tectônicos, Rodovia MGT 367 Km 583-Diamantina, MG, ZIP Code 39100-000, Brazil

^e Universidade Federal de Minas Gerais, Centro de Pesquisas Professor Manoel Teixeira da Costa, Av. Antônio Carlos, 6627 - Belo Horizonte, MG, ZIP code 31270-901, Brazil

^f Universidade Federal de Ouro Preto, Departamento de Geologia-Escola de Minas, Laboratório de Modelagem Tectônica (LabMod), Campus Morro Do Cruzeiro, Ouro Preto, MG, ZIP code 35400-000, Brazil

^g Universidade de São Paulo, Instituto de Astronomia, Geofísica e Ciências Atmosféricas, Rua Do Matão 1226, São Paulo, SP, ZIP Code 05508-090, Brazil

ARTICLE INFO

Keywords:

Ediacaran-cambrian transition
Sedimentary trace-metal patterns
Restricted sea
Bambuí Group

ABSTRACT

The sedimentary evolution of the Bambuí foreland basin system in the interior of West Gondwana is marked by periods of connection and isolation from the global ocean during the late Neoproterozoic and early Paleozoic. To understand the link between these periods and seawater redox conditions, we present an integrated study of trace-metal geochemistry and stratigraphy of the carbonate-siliciclastic rocks from the two lowermost second order transgressive-regressive sequences of the Bambuí Group, east Brazil. The basal 2nd-order sequence trace-metal pattern shows a progressive decrease of mass fractions of Co, Cr, Ni, Cu, Mo, U, V, Zn, and Cd, concomitant with a progressive decrease of Al and Fe contents and Mo/TOC ratios. Among all these elements, only Cd, Mo and U mass fractions seem to be less or not affected by detrital influence, so they can be used as reliable redox proxies for the paleoenvironmental analysis of the studied Bambuí strata. Moreover, normalization to aluminum shows a progressive increase of trace-metal enrichments for Cd and Mo in the order of 0.1–10 times and for U in the order of 1–100 times, accompanied by a progressive increase of organic carbon content upward section. These changes in sedimentary trace-metal patterns provide evidence for the chemical evolution of basinal deep-waters, whose conditions changed progressively from suboxic-anoxic to anoxic-euxinic at the basal transgressive-regressive sequence. We suggest that the paleomarine system represented by the basal Bambuí Group has probably evolved as an intracontinental silled basin recording changes in seawater chemistry associated with redox variations and restricted hydrographic conditions. Sedimentary trace-metal patterns indicate that Bambuí epeiric sea was initially in communication with open ocean followed by the marine restriction during the transgressive and regressive cycles, respectively. This resulted in a long deepwater residence time and chemical evolution of deep watermass as a response to tectonic pulses and consequent sea-level variations during the restricted stage. Under anoxic-euxinic conditions of seawater, trace metals scarcity and micronutrient fixation limitation would have impacted nitrate bioavailability, preventing the evolution of early benthic metazoans in the Bambuí paleomarine system during the late Ediacaran and early Cambrian.

* Corresponding author.

E-mail address: grauwacka@gmail.com (C. Guacaneme).

<https://doi.org/10.1016/j.jsames.2022.103998>

Received 1 June 2022; Received in revised form 17 August 2022; Accepted 21 August 2022

Available online 28 August 2022

0895-9811/© 2022 Elsevier Ltd. All rights reserved.

1. Introduction

The Ediacaran-Cambrian transition can be considered one of the most important time intervals in the Earth System evolution, when striking changes in the ocean geochemical dynamics, extreme climate events and the appearance of the first complex animals occurred (Kaufman et al., 1997; Knoll et al., 2006; Canfield et al., 2007; Campbell and Squire, 2010; Liyuan et al., 2021). These changes are preserved in the record of sedimentary basins worldwide, whose sedimentary, geochemical and paleontological record have been interpreted in terms of changes in the global ocean-climate system (Shen et al., 1998; Marshall, 2006; Li et al., 2013; Lenton et al., 2014).

Although this scenario has been consistently described in sedimentary successions throughout the world, recent advances in the study of the stratigraphic, geochemical and paleontological record of the Ediacaran-Cambrian Bambuí Group, exposed on the São Francisco craton (east Brazil), have showed contrasting paleoenvironmental conditions coupled with the lack of typical coeval early metazoans assemblages. Carbonates from this unit present $^{87}\text{Sr}/^{86}\text{Sr}$ ratios mismatching those expected for the late Ediacaran and early Cambrian record (Paula-Santos et al., 2017; Guacaneme et al., 2021). Additionally, a basin-wide increase in Sr/Ca ratios is observed in the 2nd-order scale, preceding an extremely positive $\delta^{13}\text{C}$ excursion (Iyer et al., 1995; Caetano-Filho et al., 2021), suggesting that climate and/or tectonics induced changes in seawater chemistry of this epeiric sea, triggering local biochemical responses (Caetano-Filho et al., 2019, 2021).

The available data have pointed out that much of the Bambuí strata were deposited in a restricted foreland marine basin surrounded by the Neoproterozoic-early Paleozoic Brasiliano/Pan-African orogens in the core of West Gondwana (i.e., Paula-Santos et al., 2017; Caetano-Filho et al., 2019, 2021; Hippertt et al., 2019; Uhlein et al., 2019; Kuchenbecker et al., 2020; Guacaneme et al., 2021, Fraga-Ferreira et al., 2021; Caxito et al., 2021). This foreland basin system would have experienced intermittent periods of connection with contemporary seas (Paula-Santos et al., 2017; Caetano-Filho et al., 2019, 2020, 2021; Hippertt et al., 2019; Uhlein et al., 2019; Kuchenbecker et al., 2020; Guacaneme et al., 2021), which allowed the episodic spread of cosmopolitan organisms (e.g., *Cloudina* sp.) through an epicontinental seaway (Warren et al., 2014; Perrella et al., 2017). Conversely, the tectonically-related and progressive confinement of the basin triggered the disconnection with the global ocean which may have hampered the bloom of early animal colonization within this setting (Paula-Santos et al., 2017; Caetano-Filho et al., 2019, 2021; Hippertt et al., 2019; Guacaneme et al., 2021), considering that *Cloudina* specimens are rare in this unit and the fossil record is dominated by microbialite facies and trace fossils, and some planktic and benthic microfossil assemblages (e.g. Cruz and Nobre-Lopes, 1992; Fairchild et al., 1996; Nobre-Lopes and Coimbra, 2000; Sanchez, 2014; Sanchez et al., 2018,2020). Therefore, the Bambuí Group offers an opportunity to understand how local chemistry developed within epicontinental seas along West Gondwana interior impacted the early animal colonization.

Significant redox changes in seawater chemistry are recorded in the basal strata of the Bambuí Group, which has been interpreted as the consequence of its unusual restricted paleoenvironmental conditions. It has been suggested that the lack of oceanic connection prevented the resupply of sulfate, trace metals, micronutrients, and ultimately dissolved O_2 , leading to a decrease in the available oxygen and preventing the evolution of typical Cambrian benthic ecosystems (Hippertt et al., 2019; Caetano-Filho et al., 2021; Caxito et al., 2021). However, basin-wide detailed approaches to these subjects are still scarce. It is especially the case of trace metal-based studies, which have been proved powerful proxies to reconstruct redox evolution of seawater and hydrographic changes in ancient paleomarine systems, besides representing chemical elements essential for the metabolic pathways of organisms, including metazoans (e.g., Anbar and Knoll, 2002; Tribovillard et al., 2006; Algeo and Tribovillard, 2009; Algeo et al., 2012; Algeo and Rowe, 2012).

Here, we present a basin-scale geochemical study of trace metals (Co, Cr, Ni, Cu, Mo, U, V, Zn, and Cd) and major elements (Al, Fe, and Mn) in a high-resolution sampling of mixed carbonate-siliciclastic rocks of the Ediacaran-Cambrian Bambuí Group, aiming to better understand how tectonic and hydrographic changes may have impacted the biogeochemical cycles in late Ediacaran-early Cambrian epeiric seas, preceding the Cambrian explosion of life, by exploring the controls over the redox sensitive trace-metals within this setting. Combined with the available sequence stratigraphy framework, chemostratigraphic and paleotectonic reconstructions (e.g., Reis and Suss, 2016; Caetano-Filho et al., 2019, 2020 2021; Paula-Santos et al., 2020; Kuchenbecker et al., 2020; Guacaneme et al., 2021; Fraga-Ferreira et al., 2021), it provides valuable information for reconstructing the paleoenvironmental conditions that reigned during the unusual evolution of the Bambuí basin and similar epeiric marine systems during West Gondwana assembly.

2. Background on marine trace-metal geochemistry

Reconstructions of paleomarine systems have been improved in recent years with significant contribution from the application of trace-metal geochemistry in sedimentary rocks, which allows to assessment the redox state and chemical evolution of seawater, productivity/preservation of organic matter, the degree of hydrographic restriction in anoxic marine basins, and the deepwater residence time (Lyons et al., 2009, 2014; Algeo and Maynard, 2004, 2008; Brumsack, 2006; McManus et al., 2006; Tribovillard et al., 2006, 2012; Algeo and Tribovillard, 2009; Algeo et al., 2012; Algeo and Rowe, 2012; Sweere et al., 2016).

Trace metals (such as Co, Cr, Ni, Cu, Mo, U, V, Zn, and Cd) in seawater are less soluble under reducing conditions that may result in their overall authigenic enrichment of sedimentary successions deposited in oxygen-depleted conditions (Brumsack, 2006; Tribovillard et al., 2006, 2012; Algeo et al., 2012; Algeo and Rowe, 2012; Sansjofre et al., 2014). For example, since Mo and U are more easily scavenged or diffusively trapped across the sediment-water interface, they are often adsorbed to previously formed deposits or concentrated in minerals formed during the early diagenesis of sediments deposited under anoxic conditions (Brumsack, 2006; Tribovillard et al., 2006; Algeo and Tribovillard, 2009; Algeo and Rowe, 2012).

Mo and U are incorporated into anoxic sediments via different processes (Algeo and Maynard, 2004; Sansjofre et al., 2014). In the modern seawater, part of the dissolved U^{6+} diffuses into the sediment and is reduced to U^{4+} when it reaches the ferruginous redoxcline (where Fe^{3+} reduces to Fe^{2+}), followed by fixation into the sediments by adsorption or precipitation (Canfield and Thamdrup, 2009). This accumulation is partly mediated by bacterial sulfate reduction, which leads to uranium authigenic enrichment in marine sediments with free H_2S (Tribovillard et al., 2006, 2012; Sansjofre et al., 2014). In contrast, dissolved Mo varies little with depth, reflecting its more conservative behavior in an oxygenated water column. The reduction of Mn-oxyhydroxides liberates adsorbed Mo into pore waters through the formation of thiomolybdate (MoO_4^{2-}), which is fixed in Fe-sulfide and/or organic matter molecules, resulting in Mo sediment-enrichment in shallow burial conditions, especially in organic-matter-bearing sediments deposited in oxic seawaters. Since thiomolybdate requires free H_2S to form, Mo accumulation in the sediment occurs dominantly under euxinic (sulfidic) conditions (Zheng et al., 2000; Tribovillard et al., 2006).

The mechanisms of Mo and U accumulation into sediments in anoxic and euxinic waters are particularly well understood, which, in combination with their low detrital abundance, makes them powerful redox proxies (Algeo and Lyons, 2006; Algeo and Tribovillard, 2009; Scott and Lyons, 2012; Algeo and Rowe, 2012). U–Mo covariation patterns in marine sedimentary successions also have been strongly applied to paleogeographic reconstructions (Algeo and Tribovillard, 2009), with the use of Mo/TOC ratios to constrain both the degree of watermass restriction and the estimated time of deepwater renewal in restricted anoxic marine basins (Algeo and Rowe, 2012). The Mo/TOC ratio in the

marine sediments is proportional to the concentration of aqueous Mo in the deep watermass, showing considerable variation among restricted anoxic marine systems. For example, sediment Mo/TOC ratios and the $[Mo]_{aq}$ concentrations of the deep watermass are high in the Saanich Inlet and Cariaco Basin, and low in the Framvaren Fjord and the Black Sea. This relationship exists because in restricted marine basins with only limited resupply, removal of Mo to the sediment draws down deepwater $[Mo]_{aq}$, thus reducing the rate of removal to the sediment (Algeo and Rowe, 2012).

From a biogeochemical perspective, some trace metals are important components of enzymes and can be concentrated in modern phytoplankton (p. e., Cd, Cu, Ni and Zn). When organic matter degrades, these metals are released to the sedimentary environments and retained within organic-rich sedimentary facies (e.g., associated to early diagenetic pyrite formation), favoring their use as a reliable proxy for organic carbon sinking flux (Tribouillard et al., 2006; Sansjofre et al., 2014). Other trace-elements, such as Co and Cr, are also reduced under anoxic conditions, and they can be complexed with humic/fulvic acids. However, these elements tend to be less incorporated into authigenic sulfides, and their concentration in sediments is also associated with the abundance of clastic material, which limits their use as reliable redox proxies (Brumsack, 2006; Tribouillard et al., 2006).

Recently, trace metals have been used in carbonate rocks as novel tracers for changes in the paleoredox conditions and biochemical productivity of ancient seawater (i.e., Meyer et al., 2012; Hood et al., 2018; Yang et al., 2019; Hohl et al., 2020; Liyuan et al., 2021). Generally, trace-metal geochemical studies are focused on shale-rich samples and marine sediments with high Al content (i.e., Algeo and Maynard, 2004; Brumsack, 2006). Nevertheless, the principle for application of trace-metal geochemistry in marine carbonate rocks and their use as reliable proxies for redox and environmental conditions of seawater is similar to that of trace-metal geochemistry applied in fine-grained detrital marine rocks. Moreover, trace-metal geochemistry applied in Neoproterozoic and Cambrian marine carbonates has been successfully used as reliable proxies for seawater redox and basin environmental

conditions, despite the fact that they are composed of a mixture of organic matter, and detrital and authigenic minerals (Spangenberg et al., 2013; Sansjofre et al., 2014; Hippert et al., 2019; Usma et al., 2021).

3. Geological setting

The Ediacaran-Cambrian Bambuí Group encompasses up to 3000 m-thick marine successions of carbonate and siliciclastic rocks that cover most of the western São Francisco craton (Fig. 1A). As one of the main basin-fill units of the intracratonic São Francisco basin, these rocks unconformably overlies Meso to Neoproterozoic sedimentary successions and Archean-Paleoproterozoic basement assemblages, and are deformed within the foreland fold and thrust belts of the Brasília/Pan-African Brasília and Araçuaí orogens (Fig. 1B). The Bambuí Group has been interpreted as a record of the late stages of a foreland system (i.e., 1st-order sedimentary sequence) developed in response to the multiple overloads imposed on the São Francisco plate by the diachronic Neoproterozoic-early Paleozoic Brasília/Pan-African orogens (e.g., Martins-Neto, 2009; Alkmim et al., 2006; Alkmim and Martins-Neto, 2001, 2012; Heilbron et al., 2017; Reis et al., 2017a; Santos et al., 2000; Reis and Suss, 2016; Caxito et al., 2017; Kuchenbecker et al., 2020).

From the base to the top, the Bambuí Group includes eight formations represented (main lithology) by diamictites of the Carrancas Formation, limestones of the Sete Lagoas Formation, pelites of the Serra da Santa Helena Formation, limestones of the Lagoa do Jacaré Formation, pelites of the Serra da Saudade Formation and sandstones of the Três Marias Formation (i.e., Costa and Branco, 1961; Dardenne, 1978). Conglomerates of the Samburá and Lagoa Formosa formations occur on the western border of the basin (Castro and Dardenne, 2000; Uhlein et al., 2011, 2017), while the conglomerates and sandstones of the Gorutuba Formation and limestones of the Jaíba Formation are exclusive from the eastern border (Chiavegatto et al., 2003; Kuchenbecker et al., 2016b, 2020).

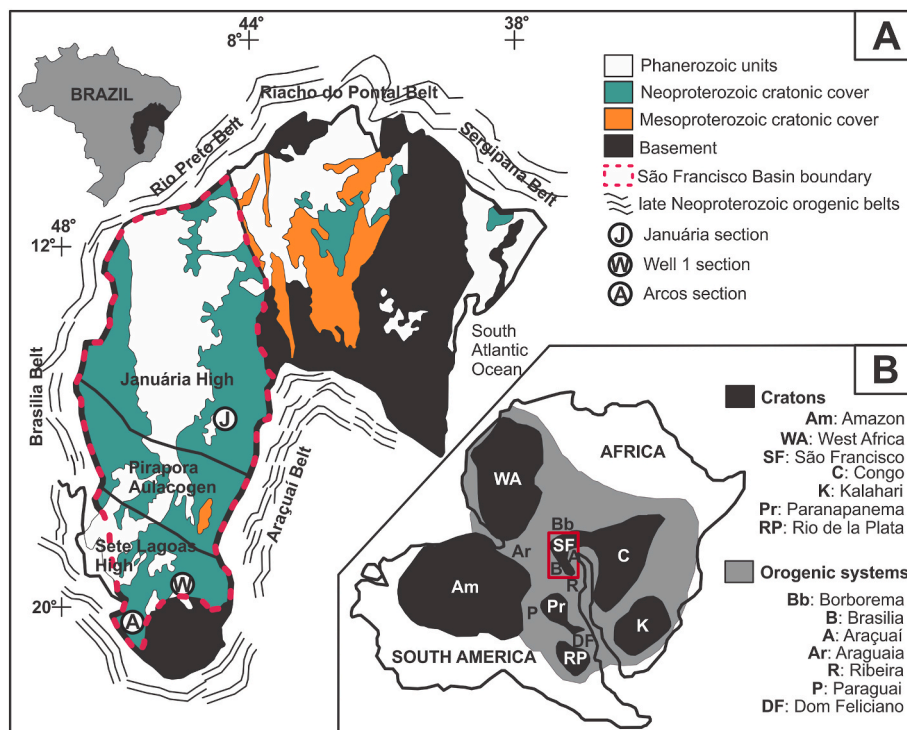


Fig. 1. (A) Geologic map of the São Francisco Craton in east Brazil and locations of the stratigraphic sections in the São Francisco Basin (B) paleogeographic reconstruction of the late Neoproterozoic West Gondwana (modified from Alkmim et al., 2006).

The Bambuí foreland system records two major depocenters, and their evolutions were mostly controlled by the Brasília orogenic system (Martins-Neto, 2009; Alkmim and Martins-Neto, 2012; Reis and Suss, 2016; Reis et al., 2017b): i) a forebulge filled with mixed carbonate-siliciclastic strata in the east; and ii) a foredeep filled with fan deltaic fine-to coarse-grained siliciclastics and minor chemical sedimentary rocks to the west. A younger and superimposed foredeep depocenter is recorded in the easternmost São Francisco basin by continental to transitional fine-to coarse-grained clastic successions. This younger depocenter is related to flexural subsidence imposed dominantly by the Araçuaí orogen to the east (Chiavegatto et al., 2003; Kuchenbecker et al., 2016b, 2020; Rossi et al., 2020).

Occurrences of the index fossil *Cloudina* sp. (Warren et al., 2014; Perrella et al., 2017) and c. 550 Ma detrital zircons (e. g., Paula-Santos et al., 2015; Kuchenbecker et al., 2020) in the Sete Lagoas Formation constrain a late Ediacaran maximum depositional age for the basal Bambuí Group. A tuff layer yielding the age of 520.2 ± 5.3 Ma within the Serra da Saudade Formation (Moreira et al., 2020), the recent discovery of the *Treptichnus Pedum* ichnofossil (Sanchez et al., 2021), and detrital zircons yielding a maximum depositional age of 527 ± 5.3 Ma (Tavares et al., 2020) in the Três Marias Formation, indicate that the deposition spanned through the Cambrian period (Fig. 2).

The known fossils from the Bambuí Group include, besides the above-mentioned taxa, microbialites, planktonic and benthic microfossils and trace fossils, mainly concentrated in the Sete Lagoas Formation (e.g. Cruz and Nobre-Lopes, 1992; Fairchild et al., 1996; Nobre-Lopes and Coimbra, 2000; Sanchez, 2014; Sanchez et al., 2018,2020). Since it is now well established that the deposition of the Bambuí Group spanned through the Cambrian, the absence of a diverse metazoan fossil fauna, abundant in countless units of this age around the world, is noteworthy. This scarcity has been explained by chemical peculiarities of the marine

environment detected by several proxies in chemostratigraphic studies, caused by the isolation of the basin from the global ocean (e.g. Paula-Santos et al., 2017, 2020; Hippertt et al., 2019; Caetano-Filho et al., 2019, 2020, 2021; Fraga-Ferreira et al., 2021; Guacaneme et al., 2021; Caxito et al., 2021). Such characteristics would have made the environment hostile to the animal diversification recorded in other Cambrian seas. Preservation problems arising from tectonic and diagenetic modification were also identified as a possible cause of the low diversity of microfossils in the sedimentary rocks of the Bambuí Group (Sanchez, 2014).

In terms of sequence stratigraphy, the Bambuí Group encompasses four transgressive-regressive 2nd-order sequences (e.g., Vieira et al., 2007b; Martins and Lemos, 2007; Reis and Suss, 2016; Reis et al., 2017a, b; Caetano Filho et al., 2019). This work focuses on the two basal 2nd-order sequences that are tracked throughout most of the basin (Fig. 2). The obtained geochemical data is integrated with the basin-scale $\delta^{13}\text{C}$ and Sr/Ca data coupled to the sequence stratigraphic framework provided by Caetano-Filho et al. (2019) and the chemostratigraphic zoning described by Paula-Santos et al. (2017) and Guacaneme et al. (2021), revealing the marine connection and restriction stages of the Bambuí foreland basin. Stratigraphic-chemostratigraphic intervals of main importance for this work are summarized below:

- (i) The lowermost 2nd-order sequence shows a basal transgressive system tract (TST) composed of glacial-related coarse-grained siliciclastics of the Carrancas Formation that grade upward into carbonates and pelites of the Sete Lagoas Formation, defining a retrogradational stacking pattern (Valeriano, 2017; Kuchenbecker et al., 2013, 2016a; Reis et al., 2017a; Caetano-Filho et al., 2019). Bounded by a basal erosional surface and an upper maximum flooding surface, this interval displays a low average

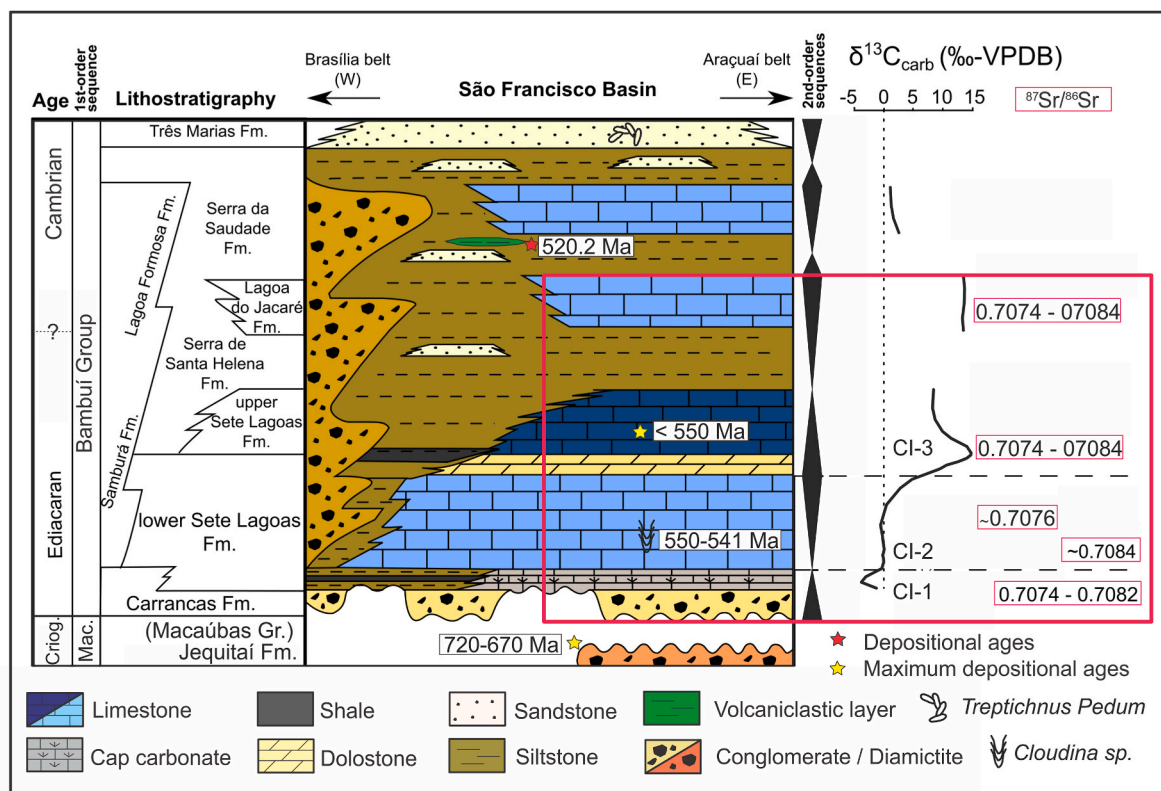


Fig. 2. Lithostratigraphic chart of the Bambuí 1st-order sequence and chemostratigraphic evolution (modified from Caetano-Filho et al., 2019). Index fossil *Cloudina* sp. in the lower Sete Lagoas Formation defines a late Ediacaran age ((Warren et al., 2014), and index ichnofossil *Treptichnus Pedum* in the Três Marias Formation defines the Ediacaran-Cambrian transition within the Bambuí Group (Sanchez et al., 2021). Maximum depositional age is represented by the yellow star at the upper Sete Lagoas Formation (Paula-Santos et al., 2015), and depositional age of a volcaniclastic layer is represented by the red star at the upper Serra da Saudade Formation; Moreira et al., 2020). Chemostratigraphic Intervals (CI) of $\delta^{13}\text{C}$ and $^{87}\text{Sr}/^{86}\text{Sr}$ are from Paula-Santos et al. (2017).

Sr/Ca ratio of 0.001, negative to positive $\delta^{13}\text{C}$ excursions from -5 to 0 ‰, an increase of $^{87}\text{Sr}/^{86}\text{Sr}$ ratios from 0.7074 to 0.7084, and some layers with aragonite pseudomorph fans associated to Neoproterozoic cap carbonates (Caetano-Filho et al., 2019; Guacaneme et al., 2021).

- (ii) This lowermost TST is overlain by a highstand systems tract (HST) that encompasses the mixed carbonate-siliciclastic successions passing upward into mid to inner carbonate ramp deposits of the Sete Lagoas Formation (Reis and Suss, 2016; Caetano-Filho et al., 2019). Presenting a progradational stacking pattern, these strata are bounded at the top by an erosional unconformity surface. This whole interval displays slightly positive $\delta^{13}\text{C}$ values between 0 and $+1$ ‰ and shows a low average Sr/Ca ratio of around 0.002. However, a basin-wide geochemical change in the Sr content and Sr/Ca ratios within the HST led to Caetano-Filho et al. (2019) to subdivide it into a basal (EHST) early highstand systems tract and an upper (LHST) late highstand systems tract. The latter records a decrease in the $^{87}\text{Sr}/^{86}\text{Sr}$ ratios to ~ 0.7076 and an increase on the Sr/Ca ratios around 0.004, reflecting marine restriction, major basin-scale paleogeographic changes and probably enhanced seawater alkalinity (Guacaneme et al., 2021; Paula-Santos et al., 2020).
- (iii) The overlying 2nd-order sequence is represented by a basal TST, consisting of carbonates of the uppermost Sete Lagoas Formation and siltstones of the basal Serra de Santa Helena, which define a retrogradational stacking pattern. Bounded at the top by another maximum flooding surface, these strata are overlain by a HST that presents siliciclastics that grade upward to the carbonate-dominated successions of the Lagoa do Jacaré Formation (Reis and Suss, 2016; Caetano-Filho et al., 2019). This interval displays an extreme positive $\delta^{13}\text{C}$ excursion that reaches values as high as

$+16$ ‰ (i.e., Iyer et al., 1995; Uhlein et al., 2019; Caetano-Filho et al., 2021), an average Sr/Ca ratio of 0.002 and variable $^{87}\text{Sr}/^{86}\text{Sr}$ ratios between 0.7074 and 0.7084 (Caetano-Filho et al., 2019; Guacaneme et al., 2021). Paleoenvironmental interpretations based on Sr isotope ratios and REY patterns suggest a significant change in the weathering regime on the marginal orogenic belts of the São Francisco craton with a preferential contribution from carbonates during the restricted stage of the basin (Paula-Santos et al., 2017, 2018; Guacaneme et al., 2021). The highly positive $\delta^{13}\text{C}$ excursion, named as the Middle Bambuí Excursion (MIBE), have been interpreted as short-lived changes in total carbon input to the basin, higher burial rates, higher carbonate authigenesis (Uhlein et al., 2019), or as a major biogeochemical turnover from predominantly sulfate-reducing to methanogenic conditions (Caetano-Filho et al., 2021) after sulfate-distillation through the basal sequence. The lack of oceanic connection would have prevented the re-supply of marine sulfate, trace elements, nutrients, and ultimately dissolved O_2 , thus leading to a decrease in the biological activity and prevented the animal evolution of a typical Cambrian ecosystem (Hippert et al., 2019; Caetano-Filho et al., 2021).

4. Methods

4.1. Studied sections

Three stratigraphic sections from the basal Bambuí Group were studied: Arcos, Well 1 and Januária sections (Fig. 3–5). On the Sete Lagoas High, southern portion of the basin, the Arcos and Well 1 sections were constructed based on the interpretation of two drill cores previously studied by Kuchenbecker et al. (2016a) and Reis and Suss (2016),

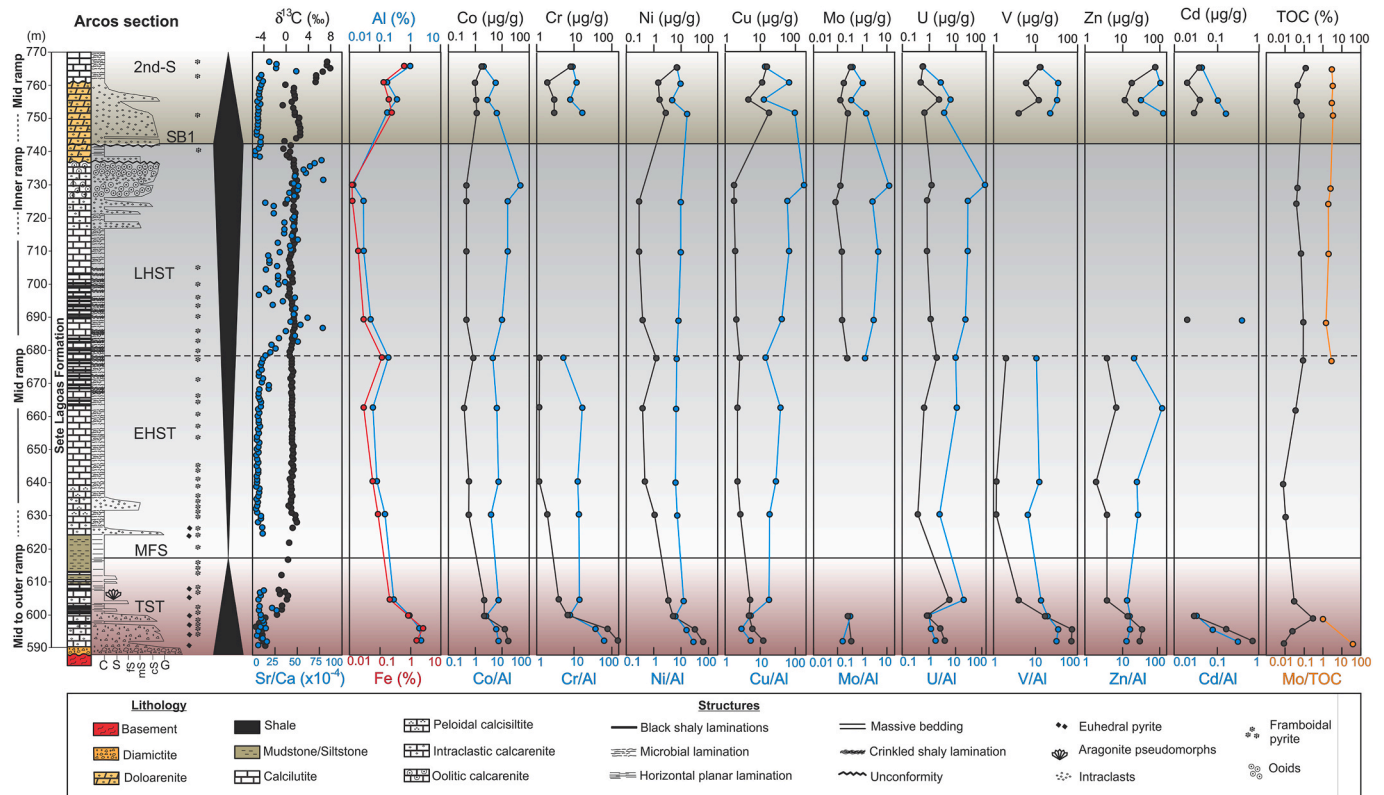


Fig. 3. Arcos section showing integrated sequence stratigraphy and chemostratigraphy of $\delta^{13}\text{C}$ values and Sr/Ca ratios from Caetano-Filho et al. (2019), TOC contents from Caetano-Filho et al. (2021), and Mo/TOC ratios, Al and Fe contents, trace-metal mass fractions and enrichments (modified from Caetano-Filho et al., 2019). TST – Transgressive System Tract; MFS – Maximum Flooding Surface; EHST – Early Highstand System Tract; LHST – Late Highstand System Tract; SB1 – Sequence Boundary; 2nd-S – Upper Second Order Sequence.

respectively. The Arcos section displays a ca. 175 m-thick succession that includes the Carrancas and Sete Lagoas formations, which unconformably overlie the Archean cratonic basement and represent the lowermost 2nd-order sequence and part of the overlying one (Fig. 3; Kuchenbecker et al., 2013, 2016a; Caetano-Filho et al., 2019; Bedoya-Rueda, 2019). The Well 1 section represents a ~430 m-thick and continuous succession including the Carrancas, Sete Lagoas and the basal Serra de Santa Helena formations. Comprising the lowermost 2nd-order sequence and part of the overlying succession, these units were deposited within a forebulge graben developed in the eastern foreland basin depocenter, through the reactivation of preexisting Archean-Proterozoic basement structures in the Sete Lagoas High, northern portion of the basin (Fig. 4; Reis and Suss, 2016; Reis et al., 2017a). The Januária section is a composite stratigraphic section of ~140 m-thick that is based on surface information and includes the sedimentary strata of the Sete Lagoas, Serra de Santa Helena and Lagoa do Jacaré formations, overlying basement assemblages in the Januária High (Fig. 5; Caetano-Filho et al., 2019). It encompasses almost complete successions of the two lowermost 2nd order sequences of the Bambuí Group.

Detailed sedimentary facies description, sequence stratigraphy framework, and regional $\delta^{13}\text{C}$ and Sr/Ca chemostratigraphy of the three studied sections were presented by Kuchenbecker et al. (2016a), Reis and Suss (2016), and Caetano-Filho et al. (2019). Organic carbon content (TOC) from these sections was presented by Caetano-Filho et al. (2021). Part of the chemostratigraphic and TOC data presented by Caetano-Filho et al. (2019, 2021) are reproduced in Figs. 3–5.

4.2. Trace-metal geochemistry

Sixty-two rock samples from the sections Januária (n = 15), Arcos (n = 16), and Well 1 (n = 31) were analyzed for trace metal contents (Table 1). They were chosen based on previously rock samples analyzed for TOC data, as well as the stratigraphic and chemostratigraphic framework (Caetano-Filho et al., 2019, 2021). Macroscopic observations and petrographic analyses were carried out to select the more preserved areas of the rock samples, which were then crushed and pulverized using an agate mortar. The samples were analyzed using the ME-MS61 method, which comprises a four-step acid digestion with ICP instrumentation at the ALS Global laboratories, Brazil.

Each prepared sample (0.25 g) was digested with perchloric, nitric and hydrofluoric acids. The residue was leached with dilute hydrochloric acid and diluted to volume. The final solution was analyzed by the inductively coupled plasma-mass spectrometry (ICP-MS) for trace elements and inductively coupled plasma-atomic emission spectrometry (ICP-AES) for major elements. Results were corrected for spectral inter-element interferences. Analytical precision based on replicate analyses was better than 2% for all elements. Procedural blanks for Al and Fe were <0.01%, Mn < 5 $\mu\text{g/g}$, Zn < 2 $\mu\text{g/g}$, Cr and V < 1 $\mu\text{g/g}$, Cu and Ni < 0.2 $\mu\text{g/g}$, Co and U < 0.1 $\mu\text{g/g}$, Mo < 0.05 $\mu\text{g/g}$ and Cd < 0.02 $\mu\text{g/g}$. The reliability of analytical results was monitored by the analysis of the standard reference materials MRGeo08, OREAS 905, GBM908-10 and EMOG-17.

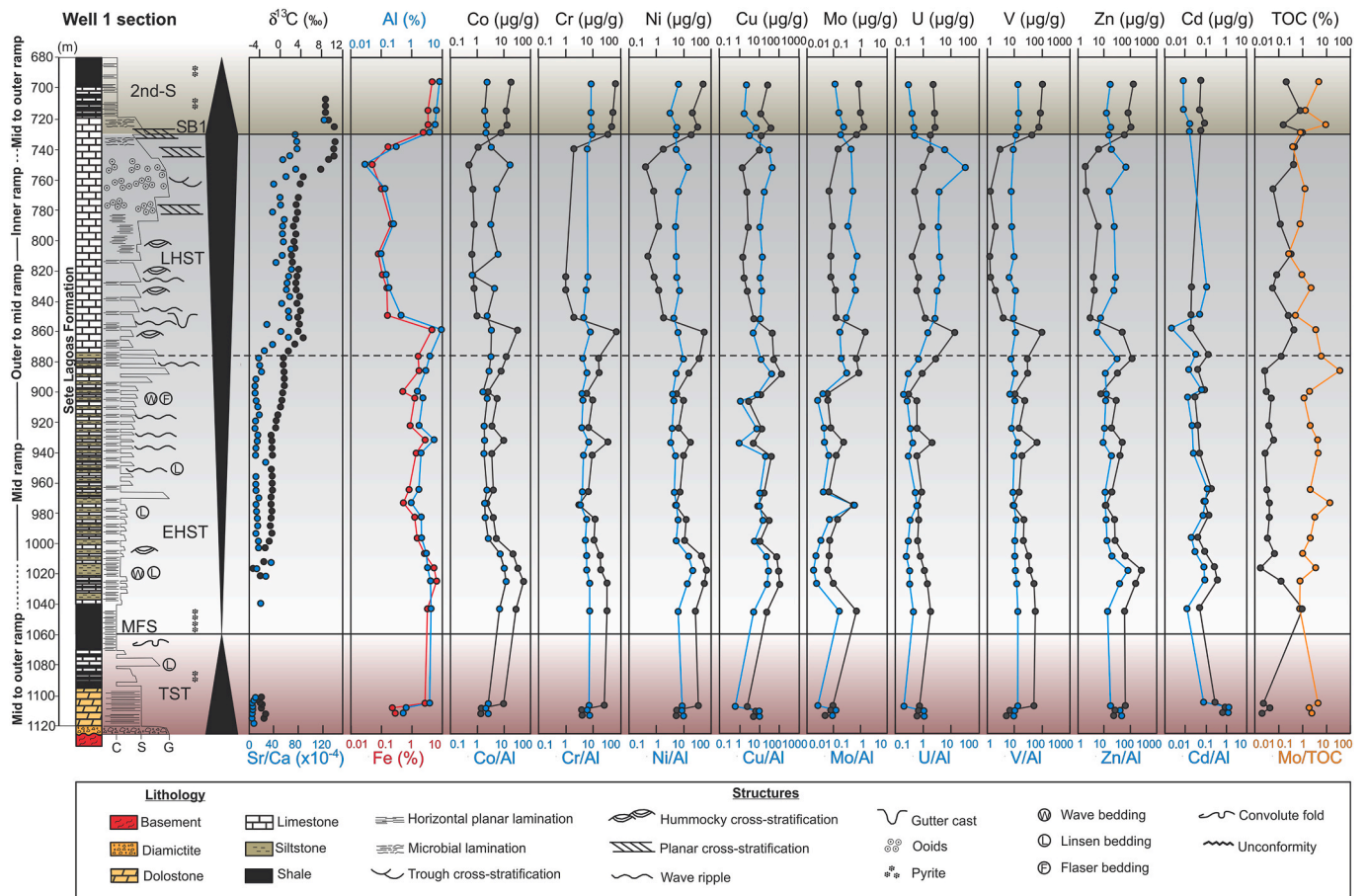


Fig. 4. Well 1 section showing integrated sequence stratigraphy and chemostratigraphy of $\delta^{13}\text{C}$ values and Sr/Ca ratios from Caetano-Filho et al. (2019), TOC contents from Caetano-Filho et al. (2021), and Mo/TOC ratios, Al and Fe contents, trace-metal mass fractions and enrichments. TST – Transgressive System Tract; MFS – Maximum Flooding Surface; EHST – Early Highstand System Tract; LHST – Late Highstand System Tract; SB1 – Sequence Boundary; 2nd-S – Upper Second Order Sequence (modified from Caetano-Filho et al., 2019).

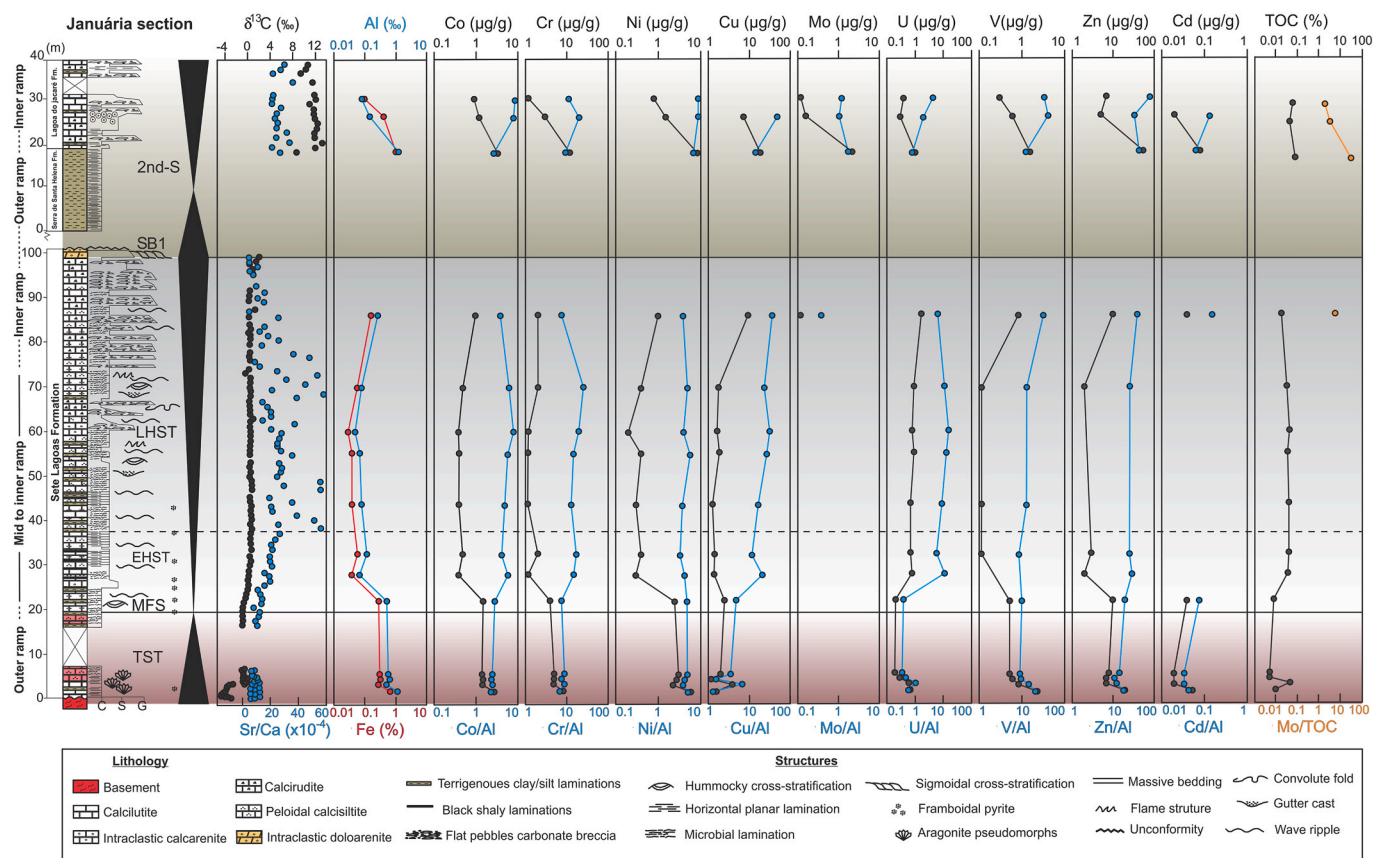


Fig. 5. Januária section showing integrated sequence stratigraphy and chemostratigraphy of $\delta^{13}\text{C}$ values and Sr/Ca ratios from Caetano-Filho et al. (2019), TOC contents from Caetano-Filho et al. (2021), and Mo/TOC ratios, Al and Fe contents, trace-metal mass fractions and enrichments. TST – Transgressive System Tract; MFS – Maximum Flooding Surface; EHST – Early Highstand System Tract; LHST – Late Highstand System Tract; SB1 – Sequence Boundary; 2nd S – Upper Second Order Sequence (modified from Caetano-Filho et al., 2019).

4.3. Normalization of trace metal data

There are several approaches for trace metal normalization in marine sediments, with the most common being division of trace metal (TM) concentrations by aluminum concentrations to account for terrigenous detrital inputs (i.e., Bennett and Canfield, 2020). This approach is subject to a number of limitations, as outlined in detail by Tribouillard et al. (2006), including the introduction of spurious correlations between element ratios that were originally uncorrelated, and the modification of genuine correlations between the original non-normalized variables. Furthermore, the use of Al as a normalizing element in sediments with low detrital inputs and high biogenic components (e.g. continental margin upwelling sediments) can lead to unrealistically high TM/Al values (Brumsack, 2006; Bennett and Canfield, 2020).

An alternative approach to Al-normalization is to calculate the excess trace metal content (TM_{XS}) of the sediments, as described by Brumsack (2006), which can provide a more reliable indicator of trace metal enrichment in sediments with low detrital inputs. However, this normalization requires knowledge of the metal to aluminum ratio in the detrital fraction of the sediment, which is often unknown, and the average crustal value used can introduce error when an environment receives terrigenous inputs that differ from the average crustal composition. The same limitation exists with enrichment factors (EF) calculated by division of TM/Al values by the crustal average (i.e., Post-Archean Australian Shale – PAAS from Taylor and McLennan, 1985), or even by the Average Crustal Carbonatic Rocks – ACCR from Turekian and Wedepohl (1961). In this study we compare trace metal concentrations from a wide variety of lithology from the Bambuí Group, comprising limestones, dolostones, mudstones, siltstones and shales,

which necessitates some form of normalization to account for the vastly different detrital inputs, considering different investigated areas of the basin as well. Given the variety of sedimentary lithology considered in this work, we argue that the use of TM/Al is the most objective approach for determining reliable trace metal enrichment patterns, as described by Bennett and Canfield (2020), and represented by the equation:

$\text{TM enrichment} = \text{Trace-metal concentration } (\mu\text{g g}^{-1}) / \text{Aluminum concentration } (\%)$

Also, the normalization of Mo concentrations to TOC values allows the comparison of levels of sedimentary enrichment among restricted marine systems containing variable amounts of organic matter, acting as a substrate for Mo uptake by the sediment (Algeo and Lyons, 2006; Algeo and Rowe, 2012). A method for estimating water mass restriction from both trace metals and TOC concentrations was proposed by Algeo and Lyons (2006), based on the observation that the amount of Mo incorporated in sediments ($[\text{Mo}]_{\text{sed}}$) in anoxic marine systems depends on both source-ion availability of aqueous Mo concentration ($[\text{Mo}]_{\text{aq}}$) and the host-phase availability of sedimentary organic matter ($[\text{TOC}]_{\text{sed}}$). This can be represented by the equations:

$$[\text{Mo}]_{\text{sed}} = [\text{TOC}]_{\text{sed}} * [\text{Mo}]_{\text{aq}} \text{ or } [\text{Mo}]_{\text{sed}} / [\text{TOC}]_{\text{sed}} = [\text{Mo}]_{\text{aq}}$$

These equations indicate that the ratio of Mo to TOC in the sediment should be proportional to the concentration of aqueous Mo in the deep watermass. Where $[\text{Mo}]_{\text{aq}}$ is high due to strong deepwater renewal, $[\text{Mo}/\text{TOC}]_{\text{sed}}$ ratios will be high. Conversely, where $[\text{Mo}]_{\text{aq}}$ concentrations are low due to limited deepwater renewal, $[\text{Mo}/\text{TOC}]_{\text{sed}}$ ratios will be low.

Table 1Co, Cr, Ni, Cu, Mo, U, V, Zn and Cd mass fractions ($\mu\text{g/g}$), Al and Fe contents (%), Mn mass fractions ($\mu\text{g/g}$), and TOC contents (%) of sedimentary rocks from the Bambuí Group at the Arcos, Well 1 and Januária sections.

Section	Sample	m	Stage	Lithology	TOC (%)	Al (%)	Fe (%)	Mn	Co	Cr	Ni	Cu	Mo	U	V	Zn	Cd
Arcos	M6	594.02	TST	Calcarenites	0.009	2.26	1.68	423	17.3	144	63	12.4	0.37	4.1	72	30	0.71
	M10	597.54	TST	Calcarenites	0.024	2.09	2.75	723	13.1	78	32.6	6.2	<0.05	2.6	73	34	0.17
	M15	601.72	TST	Calcarenites	0.302	0.9	0.89	934	2.2	7	5.7	4.9	0.29	0.9	17	14	0.03
	M20	606.52	TST	Calcarenites	0.031	0.29	0.22	1100	2.2	4	3.6	5.3	<0.05	6	4	4	<0.02
	K28a	632.17	EHST	Calcarenites	0.011	0.15	0.09	33	0.6	2	1.1	2.8	<0.05	0.4	1	4	<0.02
	K30a	642.02	EHST	Calcarenites	0.008	0.08	0.06	27	0.6	1	0.5	2.3	<0.05	<0.1	1	2	<0.02
	K34c	664.17	EHST	Calclutite	0.037	0.06	0.03	16	0.4	1	0.4	2.3	<0.05	0.7	<1	7	<0.02
	K37c	679.36	EHST	Calclutite	0.092	0.19	0.12	13	0.9	1	1.3	2.7	0.25	2	2	4	<0.02
	M40	690.9	LHST	Calclutite	0.103	0.05	0.03	<5	0.5	<1	0.4	2.1	0.15	1.2	<1	<2	0.02
	M44	711.41	LHST	Calclutite	0.072	0.03	0.02	10	0.5	<1	0.3	2	0.14	0.9	<1	<2	<0.02
	M47	726.41	LHST	Calcarenites	0.040	0.03	0.01	28	0.5	<1	0.3	1.8	0.08	0.9	<1	<2	<0.02
	M48	731.41	LHST	Calcarenites	0.048	0.01	0.01	16	0.5	<1	<0.2	1.8	0.13	1.3	<1	<2	<0.02
	K52a	753.16	2nd-S	Dolostone	0.075	0.18	0.25	211	1.2	3	3	17.8	0.26	0.7	4	23	0.03
	M53	757.16	2nd-S	Dolostone	0.044	0.37	0.2	62	1.1	3	1.7	4.7	0.13	2.5	12	12	0.04
	M54	762.16	2nd-S	Dolostone	0.050	0.17	0.14	121	1	2	1.6	11.4	0.18	0.5	6	18	<0.02
M55	767.16	2nd-S	Calclutite	0.130	0.99	0.65	159	2.1	9	7.1	13.9	0.37	0.6	13	77	0.04	
Well 1	WS-02b	1112.34	TST	Dolostone	0.020	0.53	0.28	145	1.4	4	5.1	5.4	0.05	0.6	5	23	0.63
	WS-03b	1108.66	TST	Dolostone	0.044	0.65	0.23	205	1.4	4	5.4	6.9	0.08	0.7	7	25	0.84
	WS-04a	1105.51	TST	Dolostone	0.022	3.79	2.58	1520	9.9	27	33.2	2.4	0.1	0.8	52	62	0.29
	WS-18	1043.1	EHST	Shale	0.971	4.25	3.16	31,000	28.5	32	25.2	23	0.73	1.9	58	57	0.05
	WS-22	1025.1	EHST	Siltstone	0.132	4.23	6.25	7690	52	32	55.2	110	0.1	1.4	52	152	0.36
	WS-24	1015.84	EHST	Siltstone	0.017	3.24	5	13,800	32.6	19	67.4	97.1	0.06	1.1	36	249	0.26
	WS-26	1006.63	EHST	Calcsiltite	0.067	3.05	2.53	10,100	21.4	18	43.4	73	0.07	0.8	32	58	0.09
	WS-28	996.77	EHST	Calcsiltite	0.034	2.04	1.41	2740	5.2	11	10.2	11.5	0.07	0.6	21	25	0.04
	WS-31	982.43	EHST	Calclutite	0.041	1.99	1.19	2510	4	12	11.6	31.9	0.14	0.7	23	24	0.14
	WS-33	973.34	EHST	Calclutite	0.041	0.97	0.52	9210	2	3	4.2	8	0.58	0.6	9	11	0.09
	WS-35	964.3	EHST	Calclutite	0.033	1.67	0.79	4850	4	7	7.3	18.8	0.07	0.9	15	18	0.19
	WS-40	940.81	EHST	Calclutite	0.028	1.95	1.37	2080	3.6	9	9.6	39.7	0.13	0.6	19	36	0.05
	WS-42	932.21	EHST	Calclutite	0.058	5.19	2.66	1100	9.7	36	16.6	4.9	0.24	2.2	65	45	<0.02
	WS-44	922.85	EHST	Calclutite	0.039	1.75	0.86	3020	3.4	7	6.2	13.5	0.08	0.6	14	18	0.04
	WS-48	904.28	EHST	Calclutite	0.051	2.31	1.2	1070	5.5	10	9.7	2.5	0.06	0.6	24	26	0.03
	WS-49	899.7	EHST	Calclutite	0.031	1.48	0.5	1140	2.6	6	5.5	12.2	0.06	0.3	10	11	0.09
	WS-52	886.04	EHST	Calclutite	0.026	2.92	1.69	1100	7.9	17	14.9	138	0.92	0.9	30	32	0.04
	WS-54	876.74	LHST	Calclutite	0.126	3.77	1.56	3770	11.9	16	36.3	48.8	0.74	2.7	29	113	0.13
	WS-58	859.12	LHST	Calclutite	0.445	9.01	4.44	108	30.3	72	54.8	44.9	1.59	13.6	101	48	0.02
	WS-60	850.11	LHST	Calclutite	0.256	0.43	0.16	55	1	2	1.8	5.2	0.13	1.2	4	3	0.02
	WS-64	832.03	LHST	Calclutite	0.055	0.18	0.15	74	0.8	1	1.2	2.5	0.12	0.6	2	4	0.02
WS-66	822.75	LHST	Calclutite	0.086	0.15	0.11	52	0.7	1	0.8	1.7	0.08	0.7	1	4	<0.02	
WS-69	809.01	LHST	Calclutite	0.304	0.1	0.08	65	0.6	<1	0.5	1.5	0.08	0.4	1	<2	<0.02	
WS-73	789.86	LHST	Calclutite	0.113	0.25	0.22	123	0.8	<1	1.2	2.8	0.09	0.9	2	6	<0.02	
WS-78	766.36	LHST	Calcarenites	0.059	0.13	0.1	127	0.7	<1	0.8	2.4	0.07	0.5	1	2	<0.02	
WS-81	750.45	LHST	Calcarenites	0.423	0.03	0.05	84	0.5	<1	0.4	1.4	<0.05	1	<1	2	<0.02	
WS-84	738.61	LHST	Calcarenites	0.414	0.32	0.18	66	1.1	2	1.8	10.6	0.15	1.9	3	6	<0.02	
WS-86	729.14	2nd-S	Calcarenites	0.911	3.87	2.32	780	8.1	36	19.7	12.7	0.73	1.9	44	56	0.06	
WS-87	724.45	2nd-S	Shale	0.156	5.73	3.19	448	12.9	49	31.6	40.5	1.42	2.7	79	100	0.09	
WS-89	715	2nd-S	Shale	0.805	6.39	3.27	572	12.2	55	19.8	11.3	1.02	2.6	92	78	0.05	
WS-93	695.68	2nd-S	Shale	0.195	7.78	4.46	824	18.1	66	49.1	18.1	0.9	2.3	105	128	0.06	
Januária	CM-02	1.15	TST	Calclutite	0.009	1.14	0.66	577	2.7	8	5.9	1.5	<0.05	0.7	23	20	0.05
	CM-03c	2.75	TST	Calclutite	0.044	0.57	0.28	641	1.4	5	2.3	3.9	<0.05	0.6	8	7	0.02
	CM-03h	3.87	TST	Calcsiltite	0.006	0.64	0.35	237	1.5	5	2.8	1	<0.05	0.3	6	7	<0.02
	CM-04c	4.67	TST	Calcsiltite	0.005	0.56	0.33	220	1.4	5	2.9	2	<0.05	0.2	5	8	0.02
	CM-12	21.5	EHST	Calcsiltite	0.008	0.52	0.3	204	1.5	4	2.5	2.5	<0.05	0.2	5	10	0.04
	CM-18	27.5	EHST	Calcsiltite	0.037	0.07	0.04	16	0.4	1	0.3	1.4	<0.05	0.8	<1	2	<0.02
	CM-22	31.9	EHST	Calcsiltite	0.042	0.12	0.06	16	0.5	2	0.4	1.4	<0.05	0.7	1	3	<0.02
	CM-32	43.1	LHST	Calcsiltite	0.043	0.08	0.04	15	0.4	1	0.3	1.3	<0.05	0.7	1	<2	<0.02
	CM-42	54.5	LHST	Calcsiltite	0.034	0.07	0.04	12	0.4	1	0.4	1.9	<0.05	0.9	<1	<2	<0.02
	BAR-10	59.5	LHST	Calcsiltite	0.045	0.05	0.03	17	0.4	1	0.2	1.6	<0.05	0.8	<1	<2	<0.02
	BAR-20	69.5	LHST	Calcarenites	0.034	0.08	0.06	12	0.5	2	0.4	1.8	<0.05	0.9	1	2	<0.02
	BAR-35	85.7	LHST	Calcarenites	0.018	0.26	0.17	34	1	2	1	9.3	0.1	1.7	8	10	0.04
	JL-01	150	2nd-S	Siltstone	0.074	1.25	1.04	2590	3.4	12	8.5	18.4	2.22	1	15	54	0.08

(continued on next page)

Table 1 (continued)

Section	Sample	m	Stage	Lithology	TOC (%)	Al (%)	Fe (%)	Mn	Co	Cr	Ni	Cu	Mo	U	V	Zn	Cd
	JL-09	158	2nd-S	Calcarenite	0.039	0.15	0.43	94	1.2	3	1.5	7.2	0.16	0.3	6	5	0.02
	JL-13	162	2nd-S	Calcarenite	0.061	0.09	0.1	94	0.9	1	0.8	6.1	0.11	0.4	3	7	<0.02
PAAS						8.4	7.07	1400	20	100	60	75	1	0.91	140	80	0.1
ACCR						0.42	0.38	1100	20	11	20	4	0.4	2.2	20	20	0.035

5. Results

5.1. Major and trace elements

Major elements (Al, Fe, and Mn) and trace-metal concentrations (Co, Cr, Ni, Cu, Mo, U, V, Zn, and Cd) and TOC contents of sedimentary rocks from the Bambuí Group at the Arcos, Well 1, and Januária sections are presented in Table 1. Trace-metal Al-normalized data and Mo/TOC ratios are presented in Table 2. Geochemical data of the ACCR from Turkian and Wedepohl (1961), and the PAAS from Taylor and McLennan (1985) are presented in Table 1 for comparison and discussion. Trace-metal mass fractions, trace-metal/Al ratios, TOC contents and Mo/TOC ratios are plotted aside the Arcos, Well 1, and Januária sections in Figs. 3–5, respectively.

Al and Fe contents vary from 0.01 to 9.01% and from 0.01 to 6.25%, respectively; Mn concentrations vary from 5 to 31,000 $\mu\text{g/g}$ (Table 1). [Co] varies between 0.4 and 32.6 $\mu\text{g/g}$; Cr contents range from 1.0 to 144 $\mu\text{g/g}$ with some samples presenting [Cr] <1.0; Cu contents vary between 1 and 138 $\mu\text{g/g}$; Mo concentrations range from 0.07 to 2.22 $\mu\text{g/g}$ with some samples of Januária section displaying [Mo] <0.05 $\mu\text{g/g}$; [Ni] varies between 0.2 and 67.4 $\mu\text{g/g}$; [U] ranges from 0.1 to 13.1 $\mu\text{g/g}$, V contents vary between 1.0 and 105.0 $\mu\text{g/g}$, and some samples present [V] <1.0 $\mu\text{g/g}$; Zn contents vary from 2.0 to 249 $\mu\text{g/g}$, with some samples displaying [Zn] <2.0 $\mu\text{g/g}$, and [Cd] ranges from 0.02 to 0.84 $\mu\text{g/g}$, with some samples below the detection limit of 0.02 $\mu\text{g/g}$ (Table 1). Normalization of these elements to Al content show trace-metal enrichments for Cd and Mo in the order of 0.1–10 times; Co, Cr, Ni and U in the order of 1–100 times; and Cu, V and Zn in the order of 1–1000 times upward section (Table 2).

5.2. Geochemical stratigraphic trends

5.2.1. Arcos section

Rock samples from the Arcos section show high Al and Fe contents and high Co, Cr, Ni, Cu, V, and Zn mass fractions, displaying identical decreasing-increasing trends. Both Al and Fe contents progressively fall from ~2.5% at the TST to 0.01% at the top of the LHST, and then rises from 0.18 to ~0.82% at the 2nd-S (Fig. 3). Co decreases from 17.3 $\mu\text{g/g}$ at the TST to 0.5 $\mu\text{g/g}$ at the LHST and increases up to 2.1 $\mu\text{g/g}$ at the 2nd-S, accompanied by Co/Al ratios ($\mu\text{g.g}^{-1}/\%$) that progressively increase from 7.6 at the TST to 50.0 at the top of the LHST, and then fluctuate between 2.97 and 6.7 at the 2nd-S. Cr decreases from 144 $\mu\text{g/g}$ at the TST to 1 $\mu\text{g/g}$ at the top of the EHST and then rises to 9 $\mu\text{g/g}$ at the 2nd-S; Cr/Al ($\mu\text{g.g}^{-1}/\%$) ratios decrease from 63.7 at the TST to 5.5 at the EHST, then vary between 8.1 and 16.7 at the 2nd-S. Ni progressively falls from 63 $\mu\text{g/g}$ at the TST to 0.3 $\mu\text{g/g}$ at the top of the LHST and then varies to 7.1 $\mu\text{g/g}$ at the 2nd-S; Ni/Al ratios ($\mu\text{g.g}^{-1}/\%$) slightly decrease from 27.8 to 12.4 at the TST and remain as a plateau around 7.8 at the HST, then vary between 16.6 and 4.6 at the 2nd-S. Cu slightly decreases from 12.4 $\mu\text{g/g}$ at the TST to 1.8 $\mu\text{g/g}$ at the top of the LHST and then rises up to 13.9 $\mu\text{g/g}$ at the 2nd-S; while Cu/Al ratios ($\mu\text{g.g}^{-1}/\%$) progressively increase from 5.5 at the TST to 180.0 at the top of the LHST, and decrease to 14.0 at the 2nd-S. V strongly falls from 72 $\mu\text{g/g}$ at the TST to 1 $\mu\text{g/g}$ at the EHST and fluctuates between 13 and 4 $\mu\text{g/g}$ at the 2nd-S; V/Al ratios ($\mu\text{g.g}^{-1}/\%$) decrease from 31.6 at the TST to 10.5 at the EHST and range between 13.1 and 35.2 at the 2nd-S. Zn decreases

from 30 $\mu\text{g/g}$ at the TST to 2 $\mu\text{g/g}$ at the EHST, then increases from 23–77 $\mu\text{g/g}$ at the 2nd-S. Zn/Al ratios ($\mu\text{g.g}^{-1}/\%$) increase from 13.2 at the TST to 116.7 at the EHST and fluctuate between 32.4 and 127.7 at the 2nd-S (Fig. 3).

On the other hand, Mo, U, and Cd concentrations present different geochemical trends with respect to Al and Fe trends. Mo fluctuates around 0.33 $\mu\text{g/g}$ at the TST, and ranges between 0.37 and 0.08 $\mu\text{g/g}$ at the LHST and 2nd-S. Mo/Al ratios ($\mu\text{g.g}^{-1}/\%$) vary around 0.24 at the TST, then increase from 1.3 to 13.0 at the LHST and fluctuate between 0.35 and 1.44 at the 2nd-S. U fluctuates between 4.1 and 0.4 $\mu\text{g/g}$ and U/Al ratios ($\mu\text{g.g}^{-1}/\%$) progressively increase from 1.0 at the TST to 130.0 at the top of the LHST and then decrease from 6.7 to 0.61 at the 2nd-S. Cd decreases from 0.71 to 0.03 $\mu\text{g/g}$ at the TST, and ranges around 0.03 $\mu\text{g/g}$ at the LHST and 2nd-S; Cd/Al ratios ($\mu\text{g.g}^{-1}/\%$) decrease from 0.31 to 0.03 at the TST and remain around 0.18 at the LHST and 2nd-S. TOC contents vary between 0.01 and 0.03% at the TST, then progressively increase from 0.01 at the EHST to 0.13% at the 2nd-S; Mo/TOC ratios ($\mu\text{g.g}^{-1}/\%$) decrease from 38.2 to 0.9 at the TST and remain around 2.61 at the LHST and 2nd-S (Fig. 3).

5.2.2. Well 1 section

Samples from the Well 1 section show the highest Al and Fe contents and trace-metal mass fractions of sedimentary rocks from the basal Bambuí Group, exhibiting identical increasing-decreasing trends. Al and Fe contents rapidly increase from 0.53 to 3.8% and from 0.28 to 2.6% at the TST, respectively; then slightly decrease at the EHST and increase up to 9.0 and 4.4% at the EHST/LHST transition, then decrease rapidly to ~0.19 and ~0.13% at the top of the LHST, and abruptly increase again around 5.9 and 3.3% at the 2nd-S, respectively (Fig. 4).

Co increases from 1.4 to 9.9 $\mu\text{g/g}$ at the TST, slightly decreases and increases between 2.0 and 32.6 $\mu\text{g/g}$ at the EHST, then rapidly decreases to values around 0.7 $\mu\text{g/g}$ at the LHST and increases progressively up to 18.1 $\mu\text{g/g}$ at the 2nd-S. Co/Al ratios ($\mu\text{g.g}^{-1}/\%$) progressively increase from 2.1 at the TST to 16.1 at the top of the LHST, and then decrease to 1.9 at the 2nd-S. Cr abruptly increases from 4 to 27 $\mu\text{g/g}$ at the TST, slightly decreases at the EHST and increases up to 72 $\mu\text{g/g}$ at the EHST/LHST transition, then decreases rapidly to 1 $\mu\text{g/g}$ at the top of the LHST, and increases rapidly from 2 to 66 $\mu\text{g/g}$ at the 2nd-S; Cr/Al ratios show a plateau around 6.1 $\mu\text{g.g}^{-1}/\%$ in the entire stratigraphic section. Ni progressively increases from 5.1 to 33.2 $\mu\text{g/g}$ at the TST, slightly decreases at the middle EHST and increases up to 54.8 $\mu\text{g/g}$ at the EHST/LHST transition, then decrease rapidly to ~1.0 $\mu\text{g/g}$ at the top of the LHST, and abruptly increases again to 49.1 $\mu\text{g/g}$ at the 2nd-S; Ni/Al ratios fluctuate around 3.2 and 20.8 $\mu\text{g.g}^{-1}/\%$ (Fig. 4).

Cu progressively increases from 5.4 to 110 $\mu\text{g/g}$ at the TST and base of the EHST; then decreases at the middle EHST and increases up to 138 $\mu\text{g/g}$ at the EHST/LHST transition, followed by a rapid decrease to low values of 1.4 $\mu\text{g/g}$ at the LHST and fluctuates between 10.6 and 40.5 $\mu\text{g/g}$ at the 2nd-S. Cu/Al ratios show similar stratigraphic trends with [Cu] trends, ranging between 0.63 and 47.3 $\mu\text{g.g}^{-1}/\%$. Mo increases and fluctuates between 0.05 and 1.59 $\mu\text{g/g}$ at the TST and EHST, then decreases to values around 0.1 $\mu\text{g/g}$ at the LHST and varies between 0.7 and 1.4 $\mu\text{g/g}$ at the 2nd-S. Mo/Al ratios display similar trends to [Mo], ranging between 0.02 and 0.47 $\mu\text{g.g}^{-1}/\%$. U fluctuates around 0.9 $\mu\text{g/g}$ at the TST and EHST; then rapidly increases to 13.6 $\mu\text{g/g}$ at the basal LHST and decreases to values again around 0.9 $\mu\text{g/g}$ at the most LHST,

Table 2Trace metal enrichments (TM/Al) and Mo/TOC ($\mu\text{g}\cdot\text{g}^{-1}/\text{wt}\%$) and Cd/Mo ratios of sedimentary rocks from the Bambuí Group at the Arcos, Well 1 and Januária sections.

Section	Sample	m	Stage	Lithology	Carb. (%)	Co/Al	Cr/Al	Ni/Al	Cu/Al	Mo/Al	U/Al	V/Al	Zn/Al	Cd/Al	Cd/Mo	Mo/TOC
Arcos	M6	594.02	TST	Calcarenites	87.73	7.65	63.71	27.87	5.48	0.16	1.81	31.86	13.27	0.31	n.a.	n.a.
	M10	597.54	TST	Calcarenites	68.09	6.26	37.32	15.59	2.96	n.a.	1.24	34.93	16.26	0.08	1.92	38.22
	M15	601.72	TST	Calcarenites	81.29	2.44	7.77	6.33	5.44	0.32	1.0	18.89	15.55	0.03	n.a.	n.a.
	M20	606.52	TST	Calcarenites	91.14	7.58	13.79	12.41	18.27	n.a.	20.68	13.79	13.79	n.a.	0.10	0.96
	K28a	632.17	EHST	Calcarenites	95.30	4.0	13.33	7.33	18.66	n.a.	2.67	6.67	26.67	n.a.	n.a.	n.a.
	K30a	642.02	EHST	Calcarenites	98.54	7.50	12.5	6.25	28.75	n.a.	n.a.	12.5	25.0	n.a.	n.a.	n.a.
	K34c	664.17	EHST	Calclutite	98.45	6.67	16.67	6.67	38.33	n.a.	11.67	n.a.	116.67	n.a.	n.a.	n.a.
	K37c	679.36	EHST	Calclutite	97.26	4.73	5.26	6.84	14.21	1.31	10.52	10.52	21.05	n.a.	n.a.	n.a.
	M40	690.9	LHST	Calclutite	99.17	10.0	n.a.	8.0	42.00	3.0	24.0	n.a.	n.a.	0.40	0.0	2.70
	M44	711.41	LHST	Calclutite	99.51	16.67	n.a.	10.0	66.67	4.67	30.0	n.a.	n.a.	n.a.	0.13	1.45
	M47	726.41	LHST	Calcarenites	99.80	16.67	n.a.	10.0	60.0	2.67	30.0	n.a.	n.a.	n.a.	0.0	1.92
	M48	731.41	LHST	Calcarenites	99.63	50.0	n.a.	n.a.	180.0	13.0	130.0	n.a.	n.a.	n.a.	0.0	1.96
	K52a	753.16	2nd-S	Dolostone	98.37	6.67	16.67	16.67	98.89	1.44	3.89	22.22	127.78	0.17	0.0	2.67
	M53	757.16	2nd-S	Dolostone	97.77	2.97	8.10	4.59	12.70	0.35	6.75	32.43	32.43	0.11	0.11	3.45
	M54	762.16	2nd-S	Dolostone	91.65	5.88	11.76	9.41	67.05	1.05	2.94	35.29	105.88	n.a.	0.31	2.89
M55	767.16	2nd-S	Calclutite	84.50	2.12	9.09	7.17	14.04	0.37	0.60	13.13	77.78	0.040	0.11	3.54	
Well 1	WS-02b	1112.34	TST	Dolostone	95.07	2.64	7.54	9.62	10.18	0.09	1.32	9.43	43.39	1.18	0.11	2.84
	WS-03b	1108.66	TST	Dolostone	92.81	2.15	6.15	8.30	10.61	0.12	1.07	10.77	38.46	1.29	12.6	2.46
	WS-04a	1105.51	TST	Dolostone	66.57	2.61	7.12	8.75	0.63	0.02	0.21	13.72	16.35	0.07	10.5	1.80
	WS-18	1043.1	EHST	Shale	27.87	6.70	7.52	5.92	5.41	0.17	44.0	13.64	13.41	0.01	2.9	4.46
	WS-22	1025.1	EHST	Siltstone	23.06	12.29	7.56	13.04	26.00	0.02	0.33	12.29	35.93	0.08	0.07	0.75
	WS-24	1015.84	EHST	Siltstone	77.36	10.06	5.86	20.80	29.96	0.01	0.34	11.11	76.85	0.08	3.6	0.75
	WS-26	1006.63	EHST	Calcsiltite	69.47	7.01	5.90	14.22	23.93	0.02	0.26	10.49	19.01	0.02	4.33	3.46
	WS-28	996.77	EHST	Calcsiltite	80.56	2.54	5.39	5.0	5.63	0.03	0.29	10.29	12.25	0.01	1.29	1.04
	WS-31	982.43	EHST	Calclutite	86.41	2.01	6.03	5.82	16.03	0.07	0.35	11.55	12.06	0.07	0.57	2.02
	WS-33	973.34	EHST	Calclutite	53.41	2.06	3.09	4.32	8.24	0.59	0.62	9.27	11.34	0.09	1.0	3.36
	WS-35	964.3	EHST	Calclutite	36.95	2.39	4.19	4.37	11.25	0.04	0.54	8.98	10.78	0.11	0.16	13.95
	WS-40	940.81	EHST	Calclutite	62.76	1.84	4.61	4.92	20.35	0.06	0.30	9.74	18.46	0.02	2.71	2.09
	WS-42	932.21	EHST	Calclutite	51.91	1.86	6.93	3.19	0.94	0.04	0.42	12.52	8.67	n.a.	0.38	4.54
	WS-44	922.85	EHST	Calclutite	54.40	1.94	4.0	3.54	7.71	0.04	0.34	8.0	10.28	0.02	0.0	4.10
	WS-48	904.28	EHST	Calclutite	27.30	2.38	4.32	4.19	1.08	0.02	0.26	10.38	11.25	0.01	0.5	2.01
	WS-49	899.7	EHST	Calclutite	49.22	1.75	4.05	3.71	8.24	0.04	0.20	6.75	7.43	0.06	0.5	1.17
	WS-52	886.04	EHST	Calclutite	42.84	2.70	5.82	5.10	47.26	0.31	0.30	10.27	10.95	0.01	1.5	1.90
	WS-54	876.74	LHST	Calclutite	86.93	3.15	4.24	9.62	12.94	0.19	0.71	7.69	29.97	0.03	0.04	35.05
	WS-58	859.12	LHST	Calclutite	47.51	3.36	7.99	6.08	4.98	0.17	1.51	11.21	5.32	0.0	0.17	5.84
	WS-60	850.11	LHST	Calclutite	84.93	2.32	4.65	4.18	12.09	0.30	2.79	9.30	6.97	0.04	0.01	3.57
	WS-64	832.03	LHST	Calclutite	98.52	4.44	5.55	6.67	13.89	0.66	3.33	11.11	22.22	0.11	0.15	0.50
	WS-66	822.75	LHST	Calclutite	98.33	4.67	6.67	5.33	11.33	0.53	4.67	6.67	26.67	n.a.	0.17	2.15
	WS-69	809.01	LHST	Calclutite	82.82	6.0	n.a.	5.0	15.0	0.80	4.0	10.0	n.a.	n.a.	0.0	0.92
	WS-73	789.86	LHST	Calclutite	94.31	3.2	n.a.	4.8	11.2	0.36	3.6	8.0	24.0	n.a.	0.0	0.26
	WS-78	766.36	LHST	Calcarenites	78.24	5.38	n.a.	6.15	18.46	0.53	3.84	7.69	15.38	n.a.	0.0	0.79
WS-81	750.45	LHST	Calcarenites	98.97	16.66	n.a.	13.33	46.67	n.a.	33.33	n.a.	66.67	n.a.	0.0	1.18	
WS-84	738.61	LHST	Calcarenites	95.96	3.43	6.25	5.62	33.12	0.46	5.93	9.37	18.75	n.a.	0.0	0.36	
WS-86	729.14	2nd-S	Calcarenites	55.88	2.09	9.30	5.09	3.28	0.18	0.49	11.36	14.47	0.01	0.08	0.80	
WS-87	724.45	2nd-S	Shale	88.82	2.25	8.55	5.51	7.06	0.24	0.47	13.78	17.45	0.01	0.06	9.07	
WS-89	715.0	2nd-S	Shale	29.57	1.90	8.60	3.09	1.76	0.15	0.40	14.39	12.20	0.01	0.04	1.27	
WS-93	695.68	2nd-S	Shale	21.18	2.32	8.48	6.31	2.32	0.11	0.29	13.49	16.45	0.01	0.07	4.60	
Januária	CM-02	1.15	TST	Calclutite	91.98	2.36	7.01	5.17	1.31	n.a.	0.61	20.17	17.54	0.04	n.a.	n.a.
	CM-03c	2.75	TST	Calclutite	95.11	2.45	8.77	4.03	6.84	n.a.	1.05	14.03	12.28	0.03	n.a.	n.a.
	CM-03h	3.87	TST	Calcsiltite	92.64	2.34	7.81	4.37	1.56	n.a.	0.46	9.37	10.93	n.a.	n.a.	n.a.
	CM-04c	4.67	TST	Calcsiltite	90.76	2.5	8.92	5.17	3.57	n.a.	0.35	8.92	14.28	0.03	n.a.	n.a.
	CM-12	21.5	EHST	Calcsiltite	86.77	2.88	7.69	4.80	4.80	n.a.	0.38	9.61	19.23	0.07	n.a.	n.a.
	CM-18	27.5	EHST	Calcsiltite	97.61	5.71	14.28	4.28	20.0	n.a.	11.42	n.a.	28.57	n.a.	n.a.	n.a.
	CM-22	31.9	EHST	Calcsiltite	97.89	4.16	16.67	3.33	11.67	n.a.	5.83	8.3	25.0	n.a.	n.a.	n.a.
	CM-32	43.1	LHST	Calcsiltite	98.51	5.0	12.5	3.75	16.25	n.a.	8.75	12.5	n.a.	n.a.	n.a.	n.a.
	CM-42	54.5	LHST	Calcsiltite	99.10	5.71	14.28	5.71	27.14	n.a.	12.85	n.a.	n.a.	n.a.	n.a.	n.a.
	BAR-10	59.5	LHST	Calcsiltite	98.97	8.0	20.0	4.0	32.0	n.a.	16.0	n.a.	n.a.	n.a.	n.a.	n.a.

(continued on next page)

Table 2 (continued)

Section	Sample	m	Stage	Lithology	Carb. (%)	Co/Al	Cr/Al	Ni/Al	Cu/Al	Mo/Al	U/Al	V/Al	Zn/Al	Cd/Al	Cd/Mo	Mo/TOC
	BAR-20	69.5	LHST	Calcarenites	98.16	6.25	25.0	5.0	22.5	n.a.	11.25	12.5	25.0	n.a.	n.a.	n.a.
	BAR-35	85.7	LHST	Calcarenites	98.93	3.84	7.69	3.84	35.76	0.38	6.53	30.77	38.46	0.15	0.4	5.41
	JL-01	150	2nd-S	Siltstone	82.43	2.72	9.6	6.8	14.72	1.77	0.80	12.0	43.2	0.06	0.04	29.94
	JL-09	158	2nd-S	Calcarenites	95.33	8.0	20.0	10.0	48.0	1.06	2.0	40.0	33.33	0.13	0.12	4.04
	JL-13	162	2nd-S	Calcarenites	97.66	10.0	11.11	8.88	67.77	1.22	4.44	33.33	77.78	n.a.	0.0	1.80
PAAS										0.12	0.10					
ACCR										0.95	5.24					

n.a. - not analyzed.

followed by an increase up to 2.7 $\mu\text{g/g}$ at the 2nd-S. U/Al ratios ($\mu\text{g.g}^{-1}/\%$) are low around 0.44 at the TST and EHST, then progressively increase from 0.72 to 33.3 at the LHST and decrease from 5.9 to 0.3 at the 2nd-S. V strongly increases from 5 to 52 $\mu\text{g/g}$ at the TST, slightly decreases at the middle EHST and increases progressively to 101 $\mu\text{g/g}$ at the EHST/LHST transition, then abruptly decreases to 1 $\mu\text{g/g}$ at the LHST and rapidly increases up to 105 $\mu\text{g/g}$ at the 2nd-S; V/Al ratios are constant around 10.45 $\mu\text{g.g}^{-1}/\%$ for all section (Fig. 4).

Zn progressively increases from 23 to 249 $\mu\text{g/g}$ at the TST and base of the EHST; then decreases and increase up to 113 $\mu\text{g/g}$ at the EHST/LHST boundary, rapidly decreases to low values of 2 $\mu\text{g/g}$ at the LHST and increases from 56 to 128 $\mu\text{g/g}$ at the 2nd-S. Zn/Al ratios show similar stratigraphic trends with [Zn] trends, fluctuating between 43.4 and 5.3 $\mu\text{g.g}^{-1}/\%$. Cd fluctuates between 0.84 and 0.03 $\mu\text{g/g}$ at the TST and EHST, then decreases to values around 0.02 $\mu\text{g/g}$ at the LHST and slightly increases from 0.5 to 1.0 $\mu\text{g/g}$ at the 2nd-S; Cd/Al ratios show similar trends with [Cd], ranging between 1.29 and 0.01 $\mu\text{g.g}^{-1}/\%$. TOC contents progressively increase from 0.02 to 0.91% at the TST and base of the EHST; then decrease to values around 0.05% at the most EHST, then increase from 0.13 to 0.91% at the LHST and 2nd-S; while Mo/TOC ratios fluctuate between 0.26 and 35.05 $\mu\text{g.g}^{-1}/\%$ (Fig. 4).

5.2.3. Januária section

Rock samples from the Januária section show high Al and Fe contents and high Co, Cr, Ni, Cu, V, and Zn mass fractions that display identical decreasing-increasing trends, very similar to geochemical trends from the Arcos section. Al and Fe contents progressively falls at the TST and middle EHST from 1.14 to 0.07% and from 0.66 to 0.04%, respectively; then progressively increase up to 0.26 and 0.17% at the top of the LHST, and decrease from 1.25 to 0.09% and from 1.04 to 0.10% at the regressive stage of the 2nd-S, respectively (Fig. 5).

Co decreases from 2.7 $\mu\text{g/g}$ at the TST to 0.4 $\mu\text{g/g}$ at the middle part of the EHST, then progressively increases up to 1 $\mu\text{g/g}$ at the top of the LHST, and decreases from 3.4 to 0.9 $\mu\text{g/g}$ at the 2nd-S. Co/Al ratios ($\mu\text{g.g}^{-1}/\%$) progressively increase from around 2.42 at the TST to 8.0 at the top of the LHST, then increase again from 2.7 to 10.0 at the 2nd-S. Cr decreases from 8 $\mu\text{g/g}$ at the TST to 1 at the middle part of the EHST, then increases to 2 $\mu\text{g/g}$ at the top of the LHST, and then decreases from 12 to 1 $\mu\text{g/g}$ at the 2nd-S. Cr/Al ratios ($\mu\text{g.g}^{-1}/\%$) progressively rise from around 7.02 at the TST to 25.0 at the top of the LHST, then vary between 9.6 and 20.0 at the 2nd-S. Ni decreases from 5.9 at the TST to 0.3 $\mu\text{g/g}$ at the middle part of the EHST, then progressively increases up to 1.0 $\mu\text{g/g}$ at the top of the LHST, and then decreases from 8.5 to 0.8 $\mu\text{g/g}$ at the 2nd-S. Ni/Al ratios slightly vary around 5.28 $\mu\text{g.g}^{-1}/\%$ in all section. V decreases from 23 $\mu\text{g/g}$ at the TST to 1 $\mu\text{g/g}$ at the middle part of the EHST, then progressively increases up to 8 $\mu\text{g/g}$ at the top of the LHST, and then decreases from 15 to 3 $\mu\text{g/g}$ at the 2nd-S. V/Al ratios range between 40.0 and 8.9 $\mu\text{g.g}^{-1}/\%$. Zn decreases from 20 $\mu\text{g/g}$ at the TST to 2 at the middle part of the EHST, then progressively increases up to 10 $\mu\text{g/g}$ at the top of the LHST, and decreases from 54 to 7 $\mu\text{g/g}$ at the

2nd-S. Zn/Al ratios slightly increase from 17.5 to 77.4 $\mu\text{g.g}^{-1}/\%$ in all section (Fig. 5).

On the other hand, Cu, Mo, U and Cd mass fractions present different geochemical trends with respect to Al and Fe trends. Cu fluctuates between 3.9 and 1.0 $\mu\text{g/g}$ at the TST and EHST, then rapidly increases up to 9.3 $\mu\text{g/g}$ at the top of the LHST, and decreases from 18.4 to 6.1 $\mu\text{g/g}$ at the 2nd-S. Cu/Al ratios progressively increase from 1.3 to 67.8 $\mu\text{g.g}^{-1}/\%$ upward section. [Mo] are low with a value of 0.1 $\mu\text{g/g}$ at the LHST and decrease from 2.2 to 0.1 $\mu\text{g/g}$ at the 2nd-S, with Mo/Al ratios of 0.38 $\mu\text{g.g}^{-1}/\%$ at the LHST, and remain around 1.35 $\mu\text{g.g}^{-1}/\%$ at the 2nd-S. U decreases from 0.7 to 0.2 $\mu\text{g/g}$ at the TST, then increases progressively from 0.2 to 1.7 $\mu\text{g/g}$ at the HST and decreases from 1 to 0.4 at the 2nd-S. U/Al ratios ($\mu\text{g.g}^{-1}/\%$) are low around 0.62 at the TST, then increase rapidly from 0.38 to 11.4 at the EHST and remain high around 10.2 at the LHST, and then increase from 0.8 to 4.4 at the 2nd-S. Cd fluctuates between 0.05 and 0.02 $\mu\text{g/g}$ at the TST and base of the EHST, remains around 0.04 $\mu\text{g/g}$ at the top of the LHST and then decreases from 0.08 to 0.02 $\mu\text{g/g}$ at the 2nd-S. Cd/Al ratios ($\mu\text{g.g}^{-1}/\%$) show a similar trend with [Cd] trend with values around 0.05 at the TST and base of the EHST, remaining as high as 0.15 at the top of the LHST, and increase from 0.06 to 0.13 at the 2nd-S. TOC contents are low and vary between 0.005 and 0.045% at the TST, then progressively increase from 0.008 to 0.043% at the EHST, and remain around 0.044% at the LHST and 2nd-S; Mo/TOC ratios ($\mu\text{g.g}^{-1}/\%$) present a value of 5.4 at the top of the LHST and decrease from 29.9 to 1.8 at the regressive stage of the 2nd-S (Fig. 5).

6. Discussion

6.1. Detrital influence on trace-metal composition

Trace-metal content in marine sedimentary rocks is usually of both detrital and authigenic origin. The detrital influence on the trace-metal compositions in samples can be tracked by petrography and also by monitoring of Al mass fractions, since it is a common element of detrital origin and is immobile during diagenesis (Brumsack, 2006; Tribouillard et al., 2006). For the cases where the obtained trace-metal mass fractions do not deviate greatly from the PAAS concentration (i.e., Taylor and McLennan, 1985) and present positive correlations with the detrital monitors, it can be inferred that their composition is mainly of detrital origin and, thus, they cannot be used as redox proxies for paleoenvironmental reconstructions.

The detrital signals exposed above are identified in the mixed carbonate-siliciclastic rocks from the basal Bambuí Group at the Arcos, Well 1, and Januária sections. These rocks are composed mainly of limestones and dolostones that present variable proportions of detrital siliciclastic sediments (quartz and feldspar grains and some clay laminae) within a carbonate matrix (>90% of carbonate content), and by siltstones, mudstones, and shales that are mostly composed of fine-grained detrital components and organic matter.

Cross-plot diagrams of rock samples from Arcos, Well 1 and Januária sections exhibit variable concentrations of Al up to 10%, Fe up to 6.25% and Mn up to 31,000 $\mu\text{g/g}$ (Fig. 6), showing a high positive correlation between Al and Fe contents ($r = 0.88$; $p(\alpha) < 0.01$), and low positive correlations between Al and Mn contents ($r = 0.30$; $p(\alpha) < 0.01$) and between Fe and Mn contents ($r = 0.46$; $p(\alpha) < 0.01$). A strong positive

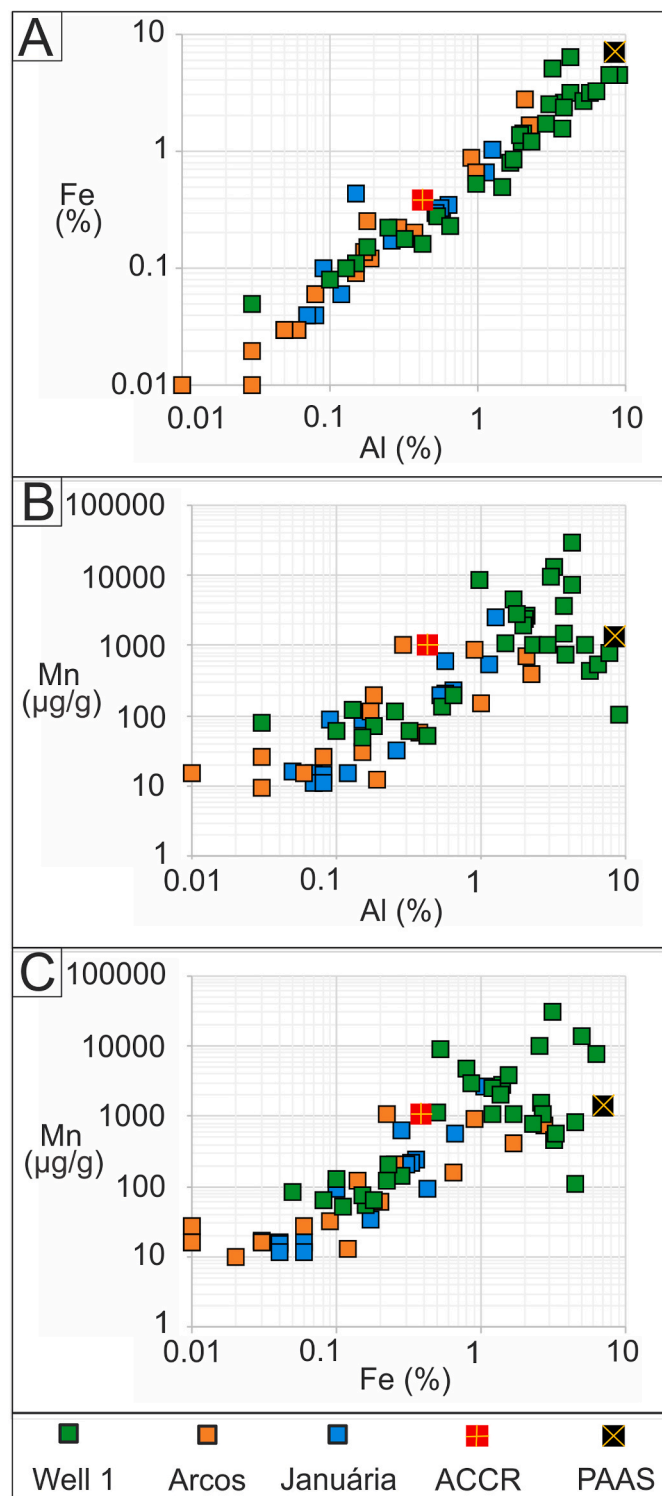


Fig. 6. Cross-plot diagrams of Al, Fe and Mn concentrations of samples from the Bambuí Group at the Arcos, Well 1, and Januária sections. PAAS values from Taylor and McLennan (1985) and ACCR values from Turekian and Wedepohl (1961) are plotted for comparison.

correlation of Fe with Al indicates a high detrital effect on the iron composition of sediments of the Bambuí Group, showing high Fe concentrations that deviate from the ACCR and point to PAAS composition (Fig. 6A), and suggesting that Fe is an element of detrital origin and, in this case, immobile during diagenesis (i.e., Brumsack, 2006; Tribouillard et al., 2006). On the other hand, the low positive correlation of Mn with Al and Fe contents suggests some degree of detrital influence on manganese composition but also displays high Mn mass fractions that deviate from the ACCR and point to PAAS values (Fig. 6A and B). Moreover, the low correlations of Mn mass fractions with Al and Fe contents also could be an effect of the high mobility of manganese during deposition and early diagenesis, which could have either escaped back to the water column or could have been trapped in authigenic Mn-carbonates or as oxides (i.e., Tribouillard et al., 2006).

In addition, cross-plot diagrams of rock samples from Arcos, Well 1, and Januária sections show variable concentrations of Co, Cr, Ni, Cu, Mo, U, V, Zn, and Cd versus Al contents (Fig. 7). Strong positive correlations of Al against V, Ni and Co mass fractions ($r = 0.93$, 0.78 and 0.73 , respectively; $p(\alpha) < 0.01$) indicate a high detrital effect on these elements (Fig. 7A, D, and 7G); positive correlations ($r = 0.66$ – 0.57 ; $p(\alpha) < 0.01$) are yielded for Al versus Cr, Zn, Mo, and U, suggesting some degree of detrital influence (Fig. 7B, E, 7H, and 7I); and low positive correlations ($r = 0.47$; $p(\alpha) < 0.01$) of Al against Cu indicate a low detrital composition effect on this element (Fig. 7F). No correlation is observed between Al versus Cd mass fractions ($r = -0.04$; $p(\alpha) > 0.01$), suggesting a negligible detrital effect on cadmium (Fig. 7C).

Cross-plot diagrams of samples from Arcos, Well 1 and Januária sections display variable concentrations of trace metals versus Fe contents (Fig. 8). Strong positive correlations of Fe against Co, Ni, V, and Zn mass fractions ($r = 0.93$ – 0.83 ; $p(\alpha) < 0.01$) indicate a high detrital effect on these elements (Fig. 8A, D, 8E and 8G); positive correlations for Fe versus Cu and Cr ($r = 0.65$ and 0.62 , respectively; $p(\alpha) < 0.01$) also suggest some degree of detrital influence (Fig. 8B and F). Nevertheless, low positive correlations of Fe against Mo and U mass fractions ($r = 0.39$ and 0.42 ; $p(\alpha) < 0.01$) indicate a low detrital composition effect on these elements (Fig. 8H and I), and no correlation is observed between Fe versus Cd mass fractions ($r = 0.09$; $p(\alpha) > 0.01$), supporting negligible detrital effect (Fig. 8C).

The detrital monitoring by [Al], together with [Fe] exhibits that Co, Cr, Ni, Cu, V and Zn mass fractions strongly deviate from the ACCR (Average Carbonatic Crustal Rocks) and point to PAAS (Post-Archean Australian Shale) composition (Figs. 7 and 8), supporting that these trace metals are mainly of detrital provenance in the sediments of the Bambuí Group and cannot be used for paleoenvironmental analysis. This is often the case for Co, but rarely for V and Ni (i. e., Jones and Manning, 1994; Tribouillard et al., 2006). Moreover, plateaus for Ni/Al ratios at Arcos and Januária sections and for Cr/Al, Ni/Al and V/Al at Well 1 section confirm the detrital influence on these elements (Fig. 3–5), whereas Mo and U are suspected to be of mixed origin (detrital and authigenic) in the sediments of the Bambuí Group. In these elements, the authigenic fraction can be estimated as the part in excess of the PAAS (i. e., Tribouillard et al., 2006; Sansjofre et al., 2014); however, the use of Al from PAAS as a normalizing element in sediments with high detrital inputs can lead to unrealistically negative authigenic fractions. Despite that Mo and U present positive correlations with [Al] and [Fe], these elements seem to be less affected by detrital sources, as evidenced by the greater deviation of samples from the PAAS, and getting closer to ACCR, suggesting authigenic enrichments of Mo and U. Moreover, mass fractions of trace metals do not correlate with the carbonate content (%) (Table 1), supporting that authigenic trace metal enrichments are not facies-dependent.

The assessment by Al monitoring, integrated with Fe monitoring shows that trace metals present a variable degree of detrital influence, which varies laterally through the Bambuí sequences, likely as a result of detrital influx from different crustal source areas (i.e., Januária and Sete Lagoas Highs, Brasília and Araçuaí orogens). Integrating these proxies, it

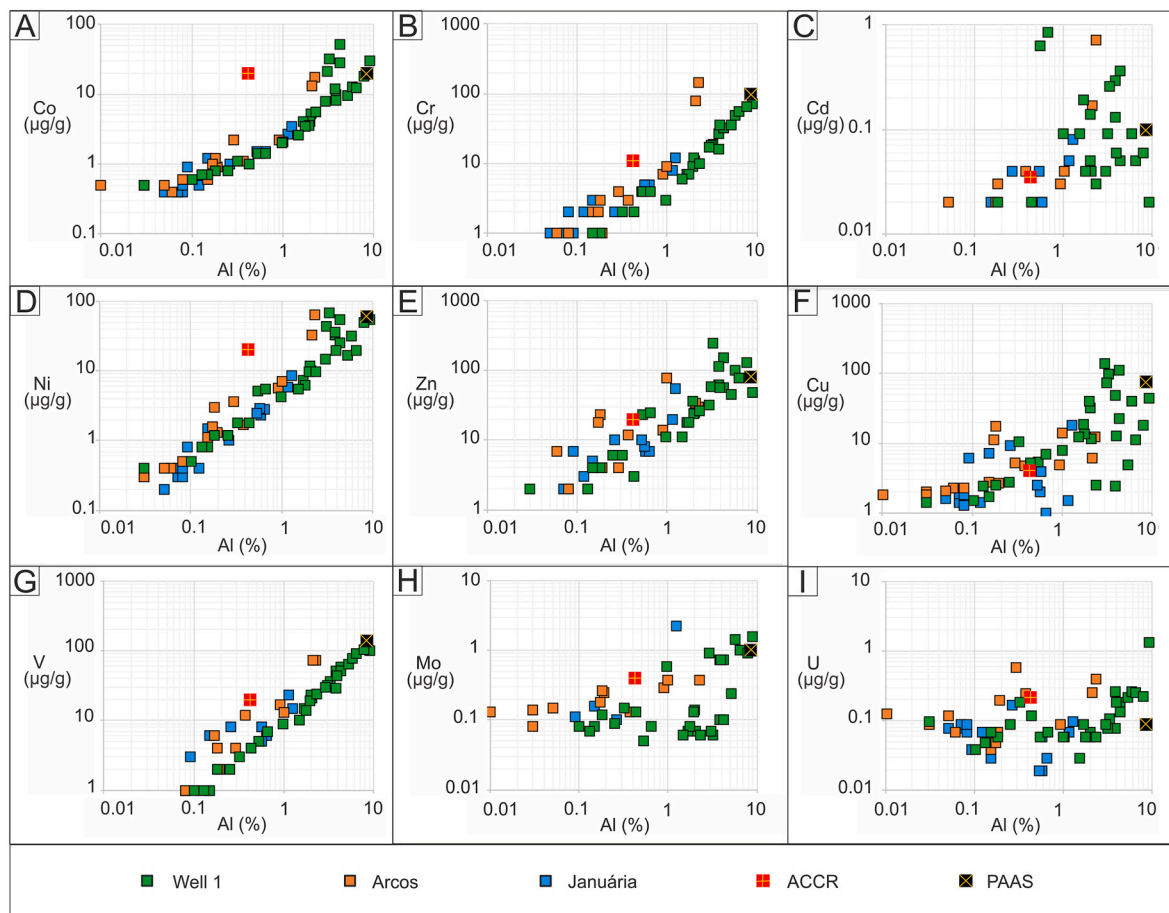


Fig. 7. Cross-plot diagrams of trace-metal mass fractions vs. Al contents of samples from the Bambuí Group at the Arcos, Well 1, and Januária sections. PAAS values from Taylor and McLennan (1985) and ACCR values from Turekian and Wedepohl (1961) are plotted for comparison.

can be concluded that Co, Cr, Ni, Cu, V, and Zn mass fractions are strongly affected by detrital influence, and these elements should not be used herein as reliable redox proxies. Nevertheless, Cd, Mo, and U mass fractions seem to be less or not affected by detrital influence. Thus, these trace metals can be used as reliable redox proxies for the paleoenvironmental analysis of the studied Bambuí strata. The wide lateral continuity of decreasing-increasing trends of trace-metal enrichments in different contexts of the basin (i.e., depth forebulge grabens and shallow basement paleohighs), represented by several carbonate facies, hinders a detrital effect over Cd, Mo and U mass fractions in these sedimentary rocks, and argues for major environmental changes in seawater at the time of deposition.

6.2. Controls on trace-metal accumulation in the epeiric bambuí sea

Generally, studies of sedimentary trace-metal composition focus on fine-grained siliciclastic samples, whereas carbonate-rich samples are excluded (i.e., Algeo and Maynard, 2004; Brumsack, 2006). Nevertheless, there are several reasons to make this approach viable in mixed carbonate-siliciclastic rocks, as addressed by other works (i.e., Meyer et al., 2012; Hood et al., 2018; Yang et al., 2019; Hohl et al., 2020; Liyan et al., 2021).

First, this study shows that authigenic fractions recorded for Cd, Mo, and U are associated with moderate to no observed correlation with Al and Fe contents and present mass fractions getting closer to Average Crustal Carbonatic Rocks (i.e., Turekian and Wedepohl, 1961). Second, other proxies applied to these rocks, such as Sr/Ca and $^{87}\text{Sr}/^{86}\text{Sr}$ ratios, REY and $\delta^{15}\text{N}$ and $\delta^{13}\text{C}$ data support chemical disturbances at the basal regressive stage in basin-scale, instead of facies-controlled trends,

similar to the observed Cd, Mo and U trends in this investigation (Caetano-Filho et al., 2019; Uhlein et al., 2019; Paula-Santos et al., 2020; Guacaneme et al., 2021; Fraga-Ferreira et al., 2021; Caxito et al., 2021). Third, trace-metal geochemistry applied in Neoproterozoic and Cambrian marine sedimentary rocks has been successfully used as reliable proxies of paleoredox and paleoenvironments of West Gondwana, although they are composed of a mixture of organic matter and detrital and authigenic minerals (i.e., Spangenberg et al., 2013; Sansjofre et al., 2014; Hippertt et al., 2019; Usma et al., 2021). Based on this, we consider that trace-metal enrichments of Cd, Mo and U recorded in the basal Bambuí Group are indicative of environmental conditions of epicontinental seawater, and other mechanisms can be suggested to explain these particular trace-metal stratigraphic trends.

Controls on the trace-metal removal from seawater to the sediment have been categorized in three main classes, based on differences in authigenic Mo–U covariation patterns of modern and ancient low-oxygen marine systems: i) benthic redox conditions; ii) operation of particulate shuttles; and iii) changes in seawater chemistry (Algeo and Tribouillard, 2009). Deep-water mass restriction can be estimated from Mo/TOC ratios (Algeo and Lyons, 2006; Lyons et al., 2009; Algeo and Rowe, 2012), and also, Cd/Mo ratios >0.1 allow the distinction between hydrographically restricted basins and upwelling-associated settings (Sweere et al., 2016). Using the contrasting stratigraphic behavior in the studied Bambuí strata, it is possible to recognize the main factors controlling the trace-metal enrichment patterns of Cd, Mo, and U for each 2nd-order systems tract.

Trace-metal patterns from the lowermost TST are indicative of sub-oxic conditions of seawater controlled by benthic redox variations (Fig. 9). Cross-plot of Mo/Al vs U/Al ratios representing authigenic

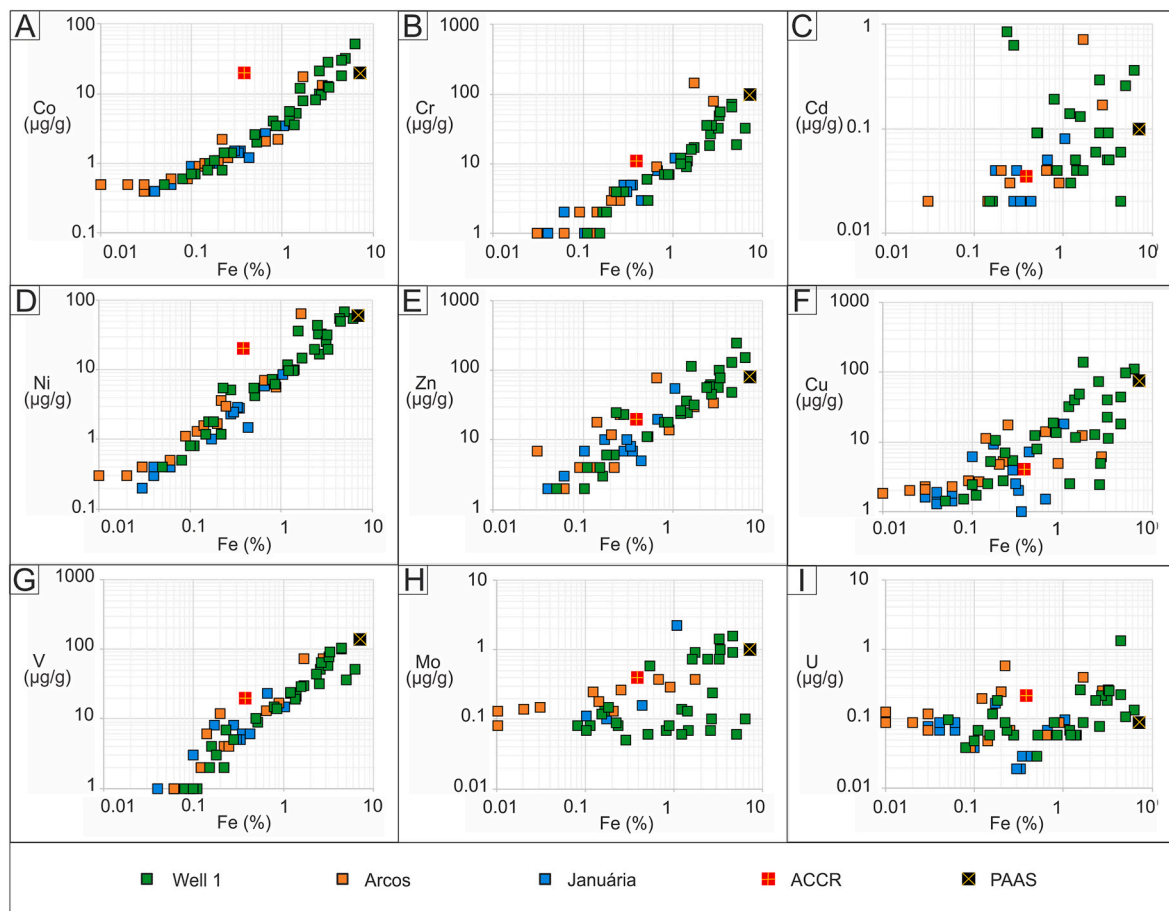


Fig. 8. Cross-plot diagrams of trace-metal mass fractions vs. Fe contents of samples from the Bambú Group at the Arcos, Well 1, and Januária sections. PAAS values from Taylor and McLennan (1985) and ACCR values from Turekian and Wedepohl (1961) are plotted for comparison.

enrichments, and analogue to enrichment factors of Mo and U (i. e., Algeo and Tribovillard, 2009; Tribovillard et al., 2012), shows trends of an open marine setting during this interval in which rates of aqueous U uptake exceeds those of aqueous Mo (Fig. 9A). This interval presents low Mo mass fractions (mean = 0.18 µg/g) and low TOC contents varying between 0.01 and 0.30% (mean = 0.05%). Mo and TOC contents exhibit a weak positive correlation ($r = 0.38$; $p(\alpha) > 0.01$) and yield relatively high Mo/TOC ratios varying between 38.23 and 1.80 (mean = 9.58). These patterns suggest that aqueous Mo concentrations were relatively high in seawater within a weakly restricted basin or open marine system that experienced watermass exchange with coeval oceans (Fig. 9B), allowing the deepwater renewal of aqueous Mo (Algeo and Lyons, 2006; Tribovillard et al., 2006, 2012; Algeo and Rowe, 2012). High Cd/Mo ratios around 5.6 exhibiting no correlation with TOC (Fig. 9C) suggest a marine environment connected with open marine systems at this stage (i.e., Sweere et al., 2016).

Suboxic and possibly sulfidic conditions controlled by benthic redox variations of seawater are recorded at the TST, in which renovation of oxygenated water column could have been a result of enhanced nutrient supply (i.e., Cd) to the Bambú seawater through the upwelling of deep ocean waters and renewal of Mo (Fig. 10A). This inference is consistent with strong but temporally variable watermass exchange across the TST and the subsequent HST of the lowermost 2nd-order sequence, in which low Sr/Ca ratios (Caetano-Filho et al., 2019), and relatively radiogenic $^{87}\text{Sr}/^{86}\text{Sr}$ ratios of ~ 0.7084 , match the Sr-isotope composition of the ocean reservoir during the late Ediacaran and early Cambrian (Guacaneme et al., 2021). The high-frequency variations of the relative sea level can be of great amplitude and higher than the long-term variations.

For basal regressive sequence (EHST), Mo/Al vs U/Al ratios show

patterns of a weakly restricted basin with a strong enrichment of Mo relative to U, which could be due to the operation of a particulate shuttle linked to Mn–redox cycling within the water column, enhancing the transfer of Mo to the seafloor, as in the modern Cariaco Basin (Algeo and Tribovillard, 2009; Tribovillard et al., 2012). These conditions result in high rates of Mo uptake that substantially exceed those of U (Fig. 9A), resulting in a large variability of sediment Mo/U ratios. This stratigraphic interval displays relatively low Mo mass fraction that varies between 0.06 and 0.92 µg/g (mean = 0.24) and low TOC contents (mean = 0.042%), except for one sample at the base of the EHST in Well 1 section that presents the highest TOC content of 0.97% (Table 1). These data show no correlation between Mo and TOC contents ($r = 0.02$; $p(\alpha) > 0.01$) (Fig. 9B), and yield relatively high Mo/TOC ratios between 0.75 and 35.05 (mean = 5.26). This suggests a substantial source of aqueous Mo in the watermass due to deepwater renewal (e.g., Algeo and Lyons, 2006; Tribovillard et al., 2006, 2012; Algeo and Rowe, 2012). Cd/Mo ratios around 1.2 exhibiting a negative correlation with TOC ($r = -0.22$; $p(\alpha) > 0.01$) could support slightly reducing conditions for this interval (Sweere et al., 2016, Fig. 9C).

The effectiveness of a particulate shuttle in promoting Mo accumulation in the EHST may be enhanced by variations in water-column redox conditions at intermediate timescales and implies that seawater in this stage starts to experience frequent redox fluctuations between suboxic, anoxic, and moderately sulfidic conditions (i.e., Algeo and Tribovillard, 2009). A weakly restricted basin scenario during the EHST is coherent with the start of a progressive decrease of the $^{87}\text{Sr}/^{86}\text{Sr}$ ratios due to poor watermass exchange (Fig. 10B), which caused the Bambú watermass to change progressively and differ from the Sr-isotope compositions of the ocean reservoir (Guacaneme et al., 2021). Also,

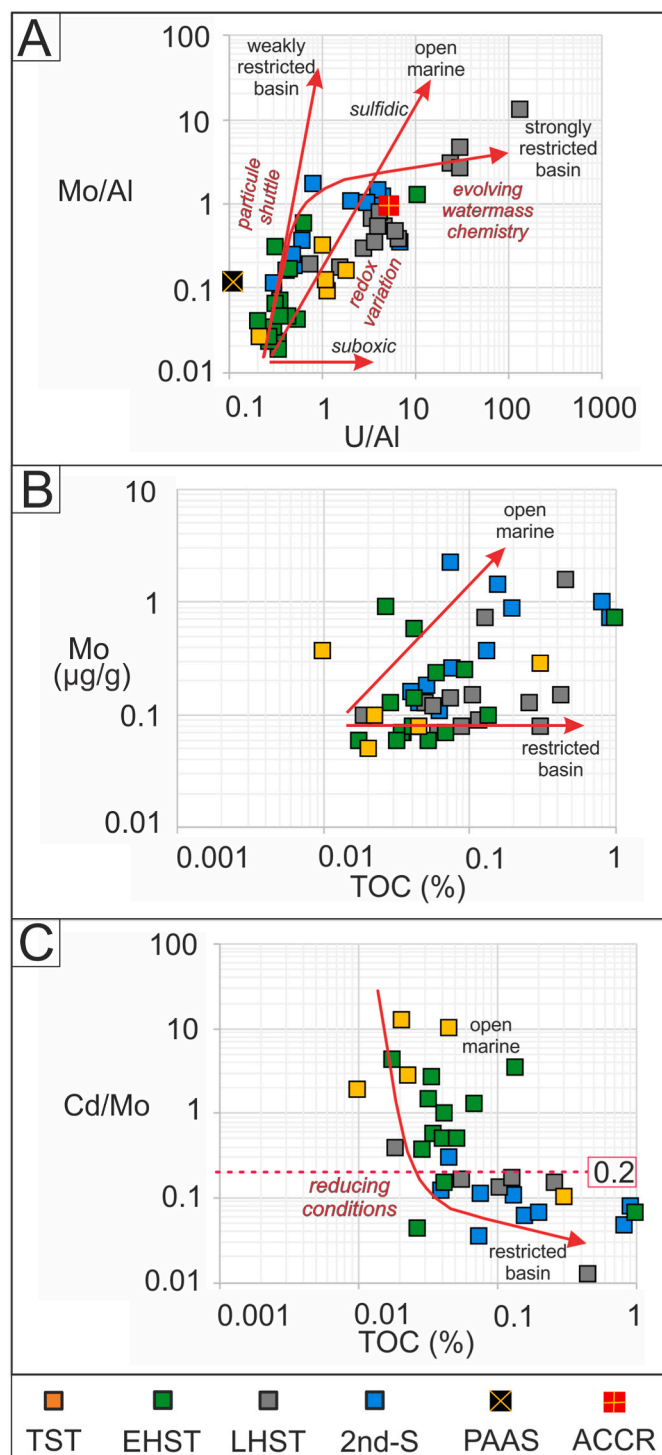


Fig. 9. Trace-metals patterns of the basal Bambuí 2nd-order sequence. (A) Mo/Al versus U/Al ratios (B) Mo mass fractions versus TOC contents (C) Cd/Mo ratios versus TOC contents. TST – Transgressive System Tract; EHST – Early Highstand System Tract; LHST – Late Highstand System Tract; 2nd S – Upper Second Order Sequence. Mo/Al and U/Al ratios of the PAAS from Taylor and McLennan (1985) and ACCR from Turekian and Wedepohl (1961) are plotted for comparison.

stratigraphic changes in trace-metal patterns and Mo/TOC ratios are likely to be controlled by abrupt changes in the redox state of depositional environment or major changes in lithology (i.e., Algeo and Rowe, 2012).

In the case of the LHST, trace-metal patterns of Mo/Al and U/Al

ratios could indicate deposition under anoxic-euxinic conditions in the water column within a strongly restricted basin (Fig. 9A), showing authigenic Mo–U covariation patterns similar to the modern Black Sea (e.g., Algeo and Tribouillard, 2009). These strata display relatively high Mo mass fractions (mean = 0.26 µg/g) and higher TOC contents varying between 0.02 and 0.42% (mean = 0.14%) that are well correlated ($r = 0.55$; $p(\alpha) < 0.01$), and yield low Mo/TOC ratios varying between 0.26 and 5.42 (mean = 2.07). These patterns show a significant drawdown of aqueous Mo concentrations in the deep watermass owing to a strong restriction (Fig. 9B), in which substantially less dissolved Mo is available for uptake by sediments compared with the underlying TST and EHST. Low Cd/Mo ratios around 0.17 present a negative correlation with TOC ($r = -0.77$; $p(\alpha) > 0.01$), and support a restricted basin, indicating expansion reducing conditions in this interval (Fig. 9C; Sweere et al., 2016).

Trace metal patterns at this interval suggest that the Bambuí seawater was highly reducing, resulting in strong U and Mo authigenic enrichments associated with anoxic-euxinic conditions developed in a confined water mass, leading to insufficient circulation and which prevent O₂ renewal (Fig. 10C). Also, intense organic matter degradation would have consumed O₂ faster than it is replenished (i.e., Tribouillard et al., 2006, 2012; Algeo et al., 2012). These successions display non-radiogenic ⁸⁷Sr/⁸⁶Sr ratios of ~0.7076 (Guacaneme et al., 2021), associated with congruent weathering and high alkalinity (Paula-Santos et al., 2020), and preceding a large positive δ¹³C excursion typical of the upper 2nd-order sequence in the middle Bambuí Group (i.e., Paula-Santos et al., 2017; Caetano-Filho et al., 2019, 2021; Hippert et al., 2019; Uhlein et al., 2019; Cui et al., 2020). In the anoxic-euxinic restrict stage recorded by the LHST, organic-rich sediment deposition probably occurred in depths below the chemocline, where trace metals are delivered to the sediments in association with organic matter decay (organometallic complexes), and trapped under intense sulfate-reducing conditions (Fig. 10C). Limited circulation patterns could have impacted the primary productivity rates due to controls on the basinal nutrient budget (i.e., Sweere et al., 2016; Caxito et al., 2021).

The upper 2nd-order sequence displays trace-metal patterns of weakly restricted basins controlled by several factors. Enrichments of Mo relative to U are probably due to the operation of Mn–particulate shuttle that enhanced the transfer of Mo to deepwater (Fig. 9A). This implies that the Bambuí seawater at this stage was affected by some degree of redox variations in the reduced water-column (i.e., Algeo and Tribouillard, 2009). This interval shows an increase in Mo contents varying from 0.11 to 2.22 µg/g (mean = 0.68 µg/g) and variable TOC contents ranging from 0.04 to 0.91% (mean = 0.23%). The correlation between Mo and TOC (Fig. 9B) is low ($r = 0.19$; $p(\alpha) > 0.01$), and Mo/TOC ratios fluctuate between 0.80 and 29.95 (mean = 5.84). Although their significance is uncertain, these relationships may reflect weak restriction (and, hence, higher aqueous Mo concentrations) of the deep watermass within the 2nd-order sequence (i.e., Algeo and Lyons, 2006; Tribouillard et al., 2006, 2012; Algeo and Rowe, 2012). However, very low Cd/Mo ratios around 0.1 suggest that the restricted stage prevails and intense reducing conditions predominate during the deposition of this interval (Fig. 9C; Sweere et al., 2016).

We argue that anoxic and possibly euxinic conditions prevailed during the deposition of the overlying 2nd-order sequence, in which sediments were intensely reduced (e.g., Caetano-Filho et al., 2021). Renewal of aqueous Mo and oxygenated waters from upwelling could have affected the chemical composition of sulfidic seawater during this basin stage (Fig. 10D); however, sulfate depletion could also have accelerated the transfer of trace metals into the sediments. The sedimentary rocks from the HST of the second sequence display extremely positive δ¹³C values up to +14%, variable high Sr/Ca ratios (Caetano-Filho et al., 2019), and variable radiogenic ⁸⁷Sr/⁸⁶Sr ratios (Guacaneme et al., 2021). Such features are associated with major disturbances in the carbon cycle and major paleoenvironmental changes in the middle Bambuí Group, which could have evolved in a predominantly sulfate

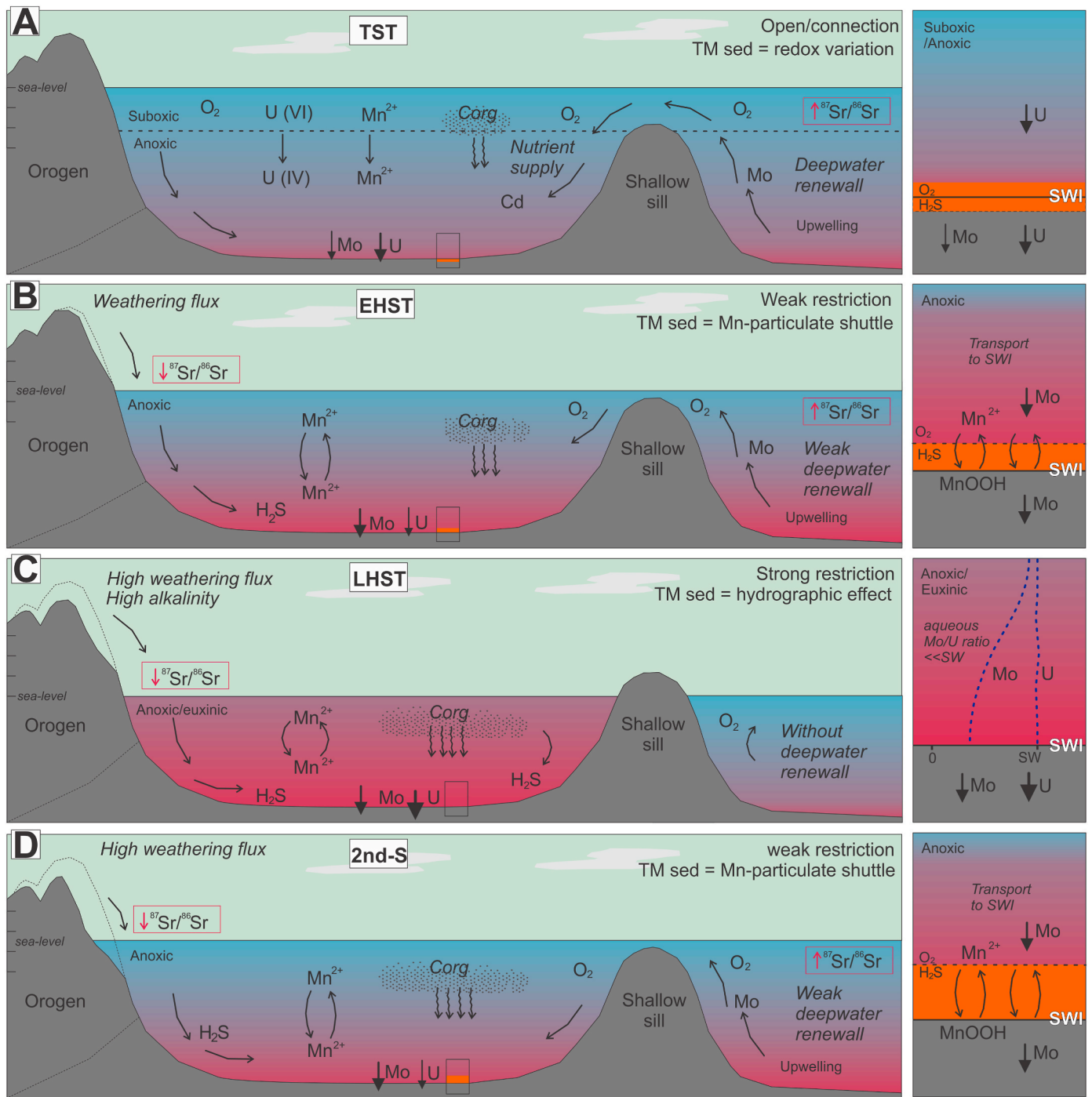


Fig. 10. Models of influences on trace-metal accumulation in different stages of the basal Bambuí 2nd-order sequence in a context of a silled basin. (A) suboxic-anoxic basin dominated by benthic redox controls, connected with open ocean and deepwater renewal by upwelling and continuous resupply of trace metals; (B) anoxic basin with weak restricted circulation dominated by Mn-particulate shuttles, (C) anoxic-euxinic basin with limited resupply of trace metals dominated by hydrographic controls and (D) anoxic basin with weak restricted circulation dominated by Mn-particulate shuttles.

limited and methanogenic environment (Cui et al., 2020; Caetano-Filho et al., 2021).

This work proposes that the Bambuí paleomarine system has evolved as an intracratonic enclosed basin in the interior of West Gondwana limited by shallow sills and orogens that hinders deepwater circulation and the exchange with oxygenated waters from the open ocean. This model of silled basin, analogous to modern anoxic silled basins (i.e., the Black Sea; Algeo and Rowe, 2012), is coherent with the stratigraphic evolution of the basal Bambuí Group, indicating that tectonically-related changes in the balance between sedimentary supply

and accommodation might have been accompanied by changes on seawater circulation and connection with the global reservoir (e.g., Reis et al., 2017; Caetano-Filho et al., 2019; Guacaneme et al., 2021). We argue that strong restriction and paleohydrographic factors likely controlled Cd, Mo, and U authigenic accumulations, as indicated by Mo/Al and U/Al ratios that deviate from the PAAS and point to ACCR composition, together with low Cd/Mo ratios <0.2 that support a restricted basin (Fig. 9). Based on above, an apparent connection was active during the deposition of the lowermost TST/EHST and partially during the deposition of the overlying 2nd-order sequence. The

mechanisms controlling these changes also resulted in a strong restriction of the Bambuí sea, the consequent long deepwater residence time, and progressively exhaustion of oxidants (i.e., Caetano-Filho et al., 2019, 2020, 2021; Kuchenbecker et al., 2020; Paula-Santos et al., 2020; Guacaneme et al., 2021).

Examining covariation patterns between trace-metal/TOC ratios and DOP (degree-of-pyritization) could assist in determining the relative importance of hydrographic versus redox influences on trace-metal accumulation in the sedimentary rocks of the Bambuí Group (i.e., Algeo and Rowe, 2012). Moreover, given that trace metal concentrations in ancient restricted seas of West Gondwana are likely to have differed from modern ocean concentrations, it is probable that trace metal enrichments in ancient sediments varied depending on the availability of trace metals in the marine reservoir (i.e., Bennett and Canfield, 2020).

6.3. Implications for the marine biota at the bambuí restricted stage

The understanding of temporal changes in the trace-metal inventory of the Bambuí paleomarine system is crucial since trace metals play essential roles on biogeochemical processes (e.g., Mo and/or V in nitrogenase, an enzyme used by nitrogen-fixing bacteria), and Cu and Zn in many other enzymes and proteins (i.e., Algeo and Rowe, 2012). Also, a comparison between trace-metal data and stable isotope proxies (i.e., $\delta^{13}\text{C}$, $\delta^{34}\text{S}$, $\delta^{15}\text{N}$) is fundamental to understanding the geochemical evolution and redox state of seawater in the Ediacaran-Cambrian Bambuí paleomarine system.

The discussion is focused on the *Cloudina*-bearing LHST (Warren et al., 2014; Perrella et al., 2017), which is marked by intense anoxic-euxinic conditions that are able to affect the availability of redox-sensitive bio-essential metals. In particular, Mo (important for biological N_2 fixation and NO_3^- assimilation) is removed from solution in H_2S -bearing waters, which are directly coupled to N bioavailability (i.e., Anbar and Knoll, 2002). The energy-intensive process of N_2 fixation, a capability limited to some bacteria and archaea, are catalyzed by nitrogenase metalloenzyme, which requires Fe and Mo as part of Fe_7MoS_9 clusters (Anbar and Knoll, 2002).

An abrupt decrease in Mo/TOC ratios occurs at the LHST and suggests a significant drawdown of bioavailable aqueous [Mo] in the deep watermass owing to strong restriction. The LHST may thus be the only interval in the Bambuí Group that records a seawater composition in which Mo is scarce. If so, the consequences for biology would have been profound. This is also consistent with N stress and scarcity of other micronutrients, such as Cd. Rates of N_2 fixation could have presumably changed the N budget during the deposition of the LHST, particularly if the use of the more efficient MoFe-nitrogenase is limited by Mo scarcity. Relevant N isotope data display increasing upward $\delta^{15}\text{N}$ values ranging from +2 to +4‰ within the lowermost HST, reflecting anoxic conditions associated with the reduction of nitrate assimilation in favor of N_2 fixation (Fraga-Ferreira et al., 2021).

Also, sedimentary pyrites in the basal Bambuí Group are progressively ^{34}S -enriched towards the LHST, suggesting that bacterial sulfate reduction strongly depleted the SO_4^{2-} reservoir in a close deep-water system of the Bambuí sea (Caetano-Filho et al., in prep.). Basin isolation led to anoxic and sulfate limited conditions, and probably resulted in a biological turnover from a sulfate-reducing to methanogenic-dominated environment through sulfate consumption by the intense activity of bacterial sulfate reduction during the regressive cycle of the basal sequence (Caetano-Filho et al., 2021; Caetano-Filho et al., in prep.). As a consequence, marine DIC would be influenced by ^{13}C -enriched methanogenic CO_2 , in the absence of sufficient amounts of methane oxidants and its loss to the atmosphere, resulting in the extreme $\delta^{13}\text{C}$ excursions in the overlying 2nd-order sequence, turning the marine environment into toxic and unfavorable conditions for colonization of benthic metazoans.

Under conditions of micro-nutrient fixation limitation during the

above-mentioned cycle, the late Ediacaran eukaryotic algae would likely have fared best in coastal and estuarine habitats where proximity to riverine metal sources minimized the effects of metal limitation, and where upwelling of NH_4^+ -bearing deep waters could have provided an adequate source of bioavailable N (i.e., Anbar and Knoll, 2002). Greatly enhanced weathering associated with the extensive Brasiliano/Pan-African orogeny at the late Ediacaran may have increased the supply of metals to seawater (Caxito et al., 2021) and could have promoted relieved N deficiency, facilitating limited eukaryotic diversification (Campbell and Squire, 2010). However, we argue that strong restriction and ultimately paleohydrographic factors likely prevented Mo renewal from deep waters by upwelling, leading to anoxic and sulfate limited conditions predominating over this marine environment at the Ediacaran-Cambrian transition. As upwelling is key for the formation of a nitrate pool, the lack of this phenomenon might have diminished the NO_3^- reservoir; consequently, eukaryotic life and benthic metazoan would not thrive in such epicontinental setting.

7. Conclusions

Changes in sedimentary trace-metal patterns of the basal Bambuí Group rocks provide evidence for the chemical evolution of basinal deep-waters, varying progressively from oxidant to reducing conditions as a response to differential rates of trace-metal removal to the sediment linked to the relative sea-level variation. A model of anoxic silled basin in the core of West Gondwana is here proposed for the Bambuí paleomarine system during the late Ediacaran and early Cambrian. Based on the chemical evolution of seawater we envisage a basin with episodic connection with open ocean controlled by the sea level variation. Connected periods were detected mainly across the TST/EHST transition of the basal 2nd order sequence (lower Sete Lagoas Formation) and partially at the TST of the overlying 2nd order sequence (upper Sete Lagoas Formation/Serra de Santa Helena Formation/Lagoa do Jacaré Formation), in which renewal of oxygenated waters and renewal of Mo from upwelling setting would have been increased. On the other hand, marine restriction during the apex of sea-level fall between the two 2nd order sequences results in extremely anoxic-euxinic conditions with long deepwater residence time and chemical evolution of deep watermass in response to tectono-eustasy. This is a possible mechanism that challenged the colonization of epicontinental seas by the early benthic metazoans at the late Ediacaran and early Cambrian. Little is known of the impacts of Mo and other trace metals on the N cycle in the past, and it is necessary to deepen knowledge of their impact on biogeochemical processes in ancient oceans.

Author statement

Cristian Guacaneme: Data curation, Writing- Original draft preparation, Conceptualization, Methodology; **Sergio Caetano-Filho:** Conceptualization and Validation; **Gustavo M. Paula-Santos:** Conceptualization and Methodology; **Marly Babinski:** Supervision, Writing-Reviewing and Editing; **Paula L. Fraga-Ferreira:** Visualization, Investigation; **Carolina Bedoya-Rueda:** Visualization, Investigation; **Mathews Kuchenbecker:** Resources, Writing- Reviewing and Editing; **Humberto L.S. Reis:** Writing - Review & Editing; **Ricardo I.F. Trindade:** Project administration and Funding acquisition.

Declaration of competing interest

The authors declare that they have no known competing financial interests or personal relationships that could have appeared to influence the work reported in this paper.

Data availability

Data will be made available on request.

Acknowledgments

Thanks to Petra company for supplying the Well 1 samples. This study was funded by the São Paulo Research Foundation (FAPESP) thematic project grant #2016/06114–6, and was also supported by CNPq grant #400764/2016–4. CAPES provided the Ph.D. fellowship to the first author. G. Paula-Santos, S. Caetano-Filho, and P.L. Fraga-Ferreira held FAPESP grants (#2017/00399–1, #2016/11496–5 and #2019/13228–6, respectively) during this work. M. Babinski, R.I.F. Trindade, and M. Kuchenbecker are fellows of the Brazilian Research Council (#307563/2013–8, #206997/2014–0, and #309106/2017–6, respectively). We would like to thank Thomas Algeo for comments on the first version of the manuscript, Reinhardt Fuck for edition support, and Giuseppina Balassone and three anonymous reviewers, whose suggestions greatly improved this paper.

References

- Anbar, A.D., Knoll, A.H., 2002. Proterozoic ocean chemistry and evolution: a bioinorganic bridge? *Science* 297, 1137–1142.
- Algeo, T.J., Lyons, T.W., 2006. Mo-total organic carbon covariation in modern anoxic marine environments: implication for analysis of paleoredox and hydrographic conditions. *Paleoceanography* 21, PA1016 23.
- Algeo, T.J., Maynard, J.B., 2004. Trace-element behavior and redox facies in core shales of Upper Pennsylvanian Kansas-type cyclothems. *Chem. Geol.* 206, 289–318.
- Algeo, T.J., Maynard, J.B., 2008. Trace metal covariation as a guide to water-mass conditions in ancient anoxic marine environments. *Geosphere* 4 (5), 872–887.
- Algeo, T.J., Rowe, H., 2012. Paleocceanographic applications of trace-metal concentration data. *Chem. Geol.* 324–325, 6–18.
- Algeo, T.J., Morford, J., Cruse, A., 2012. New applications of trace metals as proxies in marine paleoenvironments. *Chem. Geol.* 306–307, 160–164.
- Algeo, T.J., Tribouillard, N., 2009. Environmental analysis of paleocceanographic systems based on molybdenum–uranium covariation. *Chem. Geol.* 268, 211–225.
- Alkmim, F.F., Martins-Neto, M.A., 2001. A bacia intracratônica do São Francisco: arcabouço estrutural e cenários evolutivos. In: Pinto, C.P., Martins-Neto, M. (Eds.), *A Bacia do São Francisco: geologia e recursos naturais*. SBG, Belo Horizonte, pp. 9–30.
- Alkmim, F.F., Marshak, S., Pedrosa-Soares, A.C., Peres, G.G., Cruz, S., Whittington, A., 2006. Kinematic evolution of the Araçuaí-West Congo orogen in Brazil and Africa: nutcracker tectonics during the Neoproterozoic assembly of Gondwana. *Precambrian Res.* 149, 43–64.
- Alkmim, F.F., Martins-Neto, M.A., 2012. Proterozoic first-order sedimentary sequences of the São Francisco craton, eastern Brazil. *Mar. Petrol. Geol.* 33, 127–139.
- Bedoya-Rueda, C., 2019. Químiostratigrafia isotópica (C, O, Sr) de alta resolução dos carbonatos da Formação Sete Lagoas, Grupo Bambuí, na região sudoeste da Bacia do São Francisco. M.Sc. Thesis, Instituto de Geociências, Universidade de São Paulo, Brazil.
- Bennett, W.W., Canfield, D.E., 2020. Redox-sensitive trace metals as paleoredox proxies: a review and analysis of data from modern sediments. *Earth Sci. Rev.* 204, 103175.
- Brumsack, H.J., 2006. The trace metal content of recent organic carbon-rich sediments: implications for Cretaceous black shale formation. *Palaeogeogr. Palaeoclimatol. Palaeoecol.* 232, 344–361.
- Caetano-Filho, S., Paula-Santos, G.M., Guacaneme, C., Babinski, M., Bedoya-Rueda, C., Peloso, M., Amorim, K., Afonso, J., Kuchenbecker, M., Reis, H.L.S., Trindade, R.I.F., 2019. Sequence stratigraphy and chemostratigraphy of an Ediacaran-Cambrian foreland-related carbonate ramp (Bambuí Group, Brazil). *Precambrian Res.* 331, 105365.
- Caetano-Filho, S., Paula-Santos, G., Sansjofre, P., Ader, M., Cartigny, P., Guacaneme, C., Babinski, M., Kuchenbecker, M., Reis, H., Trindade, R.I.F., 2020. Eustatic control on superheavy pyrite trends from late Ediacaran-early Cambrian carbonate successions of the West Gondwana: sulfate distillation cycles in shallow water platforms?. In: *Goldschmidt Virtual 2020*.
- Caetano-Filho, S., Sansjofre, P., Ader, M., Paula-Santos, G.M., Guacaneme, C., Babinski, M., Bedoya-Rueda, C., Kuchenbecker, M., Reis, H., Trindade, R.I.F., 2021. A large epeiric methanogenic Bambuí sea in the core of Gondwana Supercontinent? *Geosci. Front.* 12, 203–218.
- Campbell, I.H., Squire, R.J., 2010. The mountains that triggered the Late Neoproterozoic increase in oxygen: the second great oxidation event. *Geochem. Cosmochim. Acta* 74 (15), 4187–4206.
- Canfield, D.E., Poulton, S.W., Narbonne, G.M., 2007. Late-Neoproterozoic deep-ocean oxygenation and the rise of animal life. *Science* 315 (5808), 92–95.
- Canfield, D.E., Thamdrup, B., 2009. Towards a consistent classification scheme for geochemical environments, or, why we wish the term ‘suboxic’ would go away. *Geobiology* 7 (4), 385–392.
- Castro, P.T.A., Dardenne, M.A., 2000. The sedimentology, stratigraphy and tectonic context of the São Francisco Supergroup at the southwestern domain of the São Francisco craton, Brazil. *Rev. Bras. Geociências* 30, 439–441.
- Caxito, F.A., Uhlein, A., Dantas, E., Stevenson, R., Egydio-Silva, M., Salgado, S.S., 2017. The rio preto and riacho do pontal belts. In: Heilbron, M., et al. (Eds.), *São Francisco Craton, Eastern Brazil*, Regional Geology Reviews. https://doi.org/10.1007/978-3-319-01715-0_12.
- Caxito, F., Lana, C., Frei, R., Uhlein, G., Sial, A., Dantas, E., Pinto, A.G., Campos, F.C., Galvão, P., Warren, L., Okubo, J., Ganade, C., 2021. Goldilocks at the dawn of complex life: mountains might have damaged Ediacaran-Cambrian ecosystems and prompted an early Cambrian greenhouse world. *Sci. Rep.* 11, 20010.
- Chiavegatto, J.R.S., Gomes, N.S., Dardenne, M.A., Delgado, C.E.R., 2003. Estratigrafia do Grupo Bambuí nas regiões do norte de Minas Gerais: Uma nova unidade estratigráfica em um contexto de inversão de bacia. In: SBG, Simpósio de Geologia de Minas Gerais, vol. 12. Ouro Preto, Anais, p. 24.
- Costa, M.T., Branco, J.R., 1961. Roteiro para a excursão Belo Horizonte-Brasília. In: Congresso Brasileiro de Geologia 14, UFMG, Inst. Pesq. Radioat., Publ. 15, 25p. Belo Horizonte.
- Cruz, N.M.C., Nobre-Lopes, J., 1992. Microfósseis do grupo Bambuí na região de Arcos, Minas Gerais. *An. Acad. Bras. Ciências* 64, 420.
- Cui, H., Warren, L.V., Uhlein, G.J., Okubo, J., Liu, X.M., Plummer, R.E., Baele, J.M., Goderis, S., Claeys, P., Li, F., 2020. Global or regional? Constraining the origins of the middle Bambuí carbon cycle anomaly in Brazil. *Precambrian Res.* 348, 105861.
- Dardenne, M.A., 1978. Síntese sobre a estratigrafia do Grupo Bambuí no Brasil Central. In: Congresso Brasileiro de Geologia, 30, Recife, vol. 2, pp. 597–610. Anais, SBG.
- Fairchild, T.R., Schopf, J.W., Shen-Miller, J., Guimarães, E.M., Edwards, M.D., Lagstein, A., Li, X., Pabst, M., Melo-Filho, L.S., 1996. Recent discoveries of Proterozoic microfossils in south-central Brazil. *Precambrian Res.* 80, 125–152.
- Fraga-Ferreira, P.L., Ader, M., Caetano-Filho, S., Sansjofre, P., Paula-Santos, G.M., Babinski, M., Guacaneme, C., Bedoya-Rueda, C., Rojas, V., Reis, H.L.S., Kuchenbecker, M., Trindade, R.I.F., 2021. The nitrogen cycle in an epeiric sea in the core of Gondwana supercontinent: a study on the ediacaran-cambrian Bambuí Group, east-central Brazil. *Front. Earth Sci.* 9, 692895.
- Guacaneme, C., Babinski, M., Bedoya-Rueda, C., Paula-Santos, G.M., Caetano-Filho, S., Kuchenbecker, M., Reis, H.L.S., Trindade, R.I.F., 2021. Tectonically-induced strontium isotope changes in ancient restricted seas: the case of the Ediacaran-Cambrian Bambuí foreland basin system, east Brazil. *Gondwana Res.* 93, 275–290.
- Heilbron, M., Cordani, U.G., Alkmim, F.F., 2017. São Francisco craton: tectonic genealogy of a miniature continent. In: *Regional Geology Reviews*. Springer, p. 326.
- Hippert, J.P., Caxito, F.A., Uhlein, G.J., Nalini, H.A., Sial, A.N., Abreu, A.T., Nogueira, L. B., 2019. The fate of a Neoproterozoic intracratonic marine basin: trace elements, TOC and IRON speciation geochemistry of the Bambuí Basin. *Brazil. Precambrian Res.* 330, 101–120.
- Hood, A.S., Planavsky, N.J., Wallace, M.W., Wang, X., 2018. The effects of diagenesis on geochemical paleoredox proxies in sedimentary carbonates. *Geochem. Cosmochim. Acta* 232, 265–287.
- Hohl, S.V., Jiang, S., Viehmann, S., Wei, W., Liu, Q., Wei, H., Galer, S.J.G., 2020. Trace metal and Cd isotope systematics of the basal Datangpo Formation, Yangtze Platform (South China) indicate restrained (bio)geochemical metal cycling in Cryogenian seawater. *Geosciences* 10, 36.
- Iyer, S.S., Babinski, M., Krouse, H.L., Chemale, F., 1995. Highly ¹³C-enriched carbonate and organic matter in the Neoproterozoic sediments of the Bambuí Group. *Brazil. Precambrian Res.* 73, 271–282.
- Jones, B., Manning, D.A.C., 1994. Comparison of geochemical indices used for the interpretation of paleoredox conditions in ancient mudstones. *Chem. Geol.* 114, 111–129.
- Kaufman, A.J., Knoll, A.H., Narbonne, G.M., 1997. Isotopes, ice ages, and terminal Proterozoic Earth history. *Proc. Natl. Acad. Sci. U.S.A.* 94, 600–605.
- Knoll, A.H., Walter, M.R., Narbonne, G.M., Christie-Blick, N., 2006. The Ediacaran Period: a new addition to the geologic time scale. *Lethaia* 39, 13–30.
- Kuchenbecker, M., Babinski, M., Pedrosa-Soares, A.C., Costa, R.D., Lopes-Silva, L., Pimenta, F., 2013. Proveniência e análise sedimentar da porção basal do Grupo Bambuí em Arcos (MG). *Geologia USP* 13 (4), 49–61.
- Kuchenbecker, M., Babinski, M., Pedrosa-Soares, A.C., Lopes-Silva, L., Pimenta, F., 2016a. Chemostratigraphy of the lower Bambuí Group, southwestern São Francisco craton, Brazil: insights on Gondwana paleoenvironments. *Braz. J. Genet.* 46, 145–162.
- Kuchenbecker, M., Atman, D., Costa, R.D., Pedrosa-Soares, A.C., Babinski, M., 2016b. A Formação Gorutuba: sedimentação litorânea a continental na margem leste da Bacia Bambuí (MG). *Geologia USP* 16 (2), 67–81.
- Kuchenbecker, M., Pedrosa-Soares, A.C., Babinski, M., Reis, H.L.S., Atman, D., Costa, R. D., 2020. Towards an integrated tectonic model for the interaction between the Bambuí basin and the adjoining orogenic belts: evidences from the detrital zircon record of syn-orogenic units. *J. S. Am. Earth Sci.* 104–102831.
- Lenton, T.M., Boyle, R.A., Poulton, S.W., Shields-Zhou, G.A., Butterfield, N.J., 2014. Co-evolution of eukaryotes and ocean oxygenation in the Neoproterozoic era. *Nat. Geosci.* 7, 257–265.
- Li, D., Ling, H.F., Shields-Zhou, G.A., Chen, X., Cremonese, L., Och, L., Manning, C.J., 2013. Carbon and strontium isotope evolution of seawater across the Ediacaran-Cambrian transition: evidence from the Xiaotan section, NE Yunnan, South China. *Precambrian Res.* 225, 128–147.
- Liyuan, W., Qingjun, G., Changqiu, Z., Rongfei, W., Yinan, D., Xiaokun, H., Liyan, T., Jing, K., Xi, Y., 2021. Trace and rare earth elements geochemistry of sedimentary rocks in the Ediacaran-Cambrian transition from the Tarim Basin, Northwest China: constrains for redox environments. *Precambrian Res.* 352, 105942.
- Lyons, T.W., Anbar, A.D., Severmann, S., Scott, C., Gill, B., 2009. Tracking euxinia in the ancient ocean: a multiproxy perspective and Proterozoic case study. *Annu. Rev. Earth Planet. Sci. Lett.* 37, 507–534.
- Lyons, T.W., Reinhard, C., Planavsky, N., 2014. The rise of oxygen in Earth’s early ocean and atmosphere. *Nature* 506, 309.
- Marshall, C.R., 2006. Explaining the Cambrian “explosion” of animals. *Annu. Rev. Earth Planet. Sci. Lett.* 34, 355–384.

- Martins, M., Lemos, V.B., 2007. Análise estratigráfica das seqüências neoproterozoicas da Bacia do São Francisco. *Rev. Bras. Geociências* 37 (4), 156–167.
- Martins-Neto, M.A., 2009. Sequence stratigraphic framework of Proterozoic successions in eastern Brazil. *Mar. Petrol. Geol.* 26, 163–176.
- McManus, J., Berelson, W.B., Severmann, S., Poulson, R.L., Hammond, D.E., Klinkhammer, G.P., Holm, C., 2006. Molybdenum and uranium geochemistry in continental margin sediments: paleoproxy potential. *Geochim. Cosmochim. Acta* 70 (4643–4662).
- Meyer, E.E., Quicksall, A.N., Landis, J.D., Link, P.K., Bostick, B.C., 2012. Trace and rare earth elemental investigation of a Sturtian cap carbonate, Pocatello, Idaho: evidence for ocean redox conditions before and during carbonate deposition. *Precambrian Res.* 192–195, 89–106.
- Moreira, D.S., Uhlein, A., Dussin, I.A., Uhlein, G.J., Misuzaki, A.M., 2020. A Cambrian age for the upper Bambuí Group, Brazil, supported by the first U–Pb dating of volcanoclastic bed. *J. S. Am. Earth Sci.* 99, 102503.
- Nobre-Lopes, J., Coimbra, A.M., 2000. Microfítolitos associados a construções estromatolíticas do Grupo Bambuí, Proterozoico Superior, região de Arcos - mg. *Rev. Bras. Precisa abreviar* 30, 589–592.
- Paula-Santos, G.M., Babinski, M., Kuchenbecker, M., Caetano-Filho, S., Trindade, R.I., Pedrosa-Soares, A.C., 2015. New evidence of an Ediacaran age for the Bambuí Group in southern São Francisco craton (eastern Brazil) from zircon U–Pb data and isotope chemostratigraphy. *Gondwana Res.* 28, 702–720.
- Paula-Santos, G.M., Caetano-Filho, S., Babinski, M., Trindade, R.I., Guacaneme, C., 2017. Tracking connection and restriction of West Gondwana São Francisco basin through isotope chemostratigraphy. *Gondwana Res.* 42, 280–305.
- Paula-Santos, G.M., Caetano-Filho, S., Babinski, M., Enzweiler, J., 2018. Rare earth elements of carbonate rocks from the Bambuí Group, southern São Francisco Basin, Brazil, and their significance as paleoenvironmental proxies. *Precambrian Res.* 305, 327–340.
- Paula-Santos, G.M., Caetano-Filho, S., Enzweiler, J., Navarro, M.S., Babinski, M., Guacaneme, C., Kuchenbecker, M., Reis, H., Trindade, R.I.F., 2020. Rare earth elements in the terminal Ediacaran Bambuí Group carbonate rocks (Brazil): evidence for high seawater alkalinity during rise of early animals. *Precambrian Res.* 336, 105506.
- Perrella, P., Uhlein, A., Uhlein, G.J., Sial, A.N., Pedrosa-Soares, A.C., Lima, O.N.B., 2017. Facies analysis, sequence stratigraphy and chemostratigraphy of the Sete Lagoas Formation (Bambuí Group), northern Minas Gerais State, Brazil: evidence of a cap carbonate deposited on the Januária basement high. *Braz. J. Genet.* 47, 59–77.
- Reis, H.L.S., Suss, J.F., 2016. Mixed carbonate-siliciclastic sedimentation in forebulge grabens: an example from the Ediacaran Bambuí Group, São Francisco basin. *Brazil. Sediment. Geol.* 339, 83–103.
- Reis, H.L.S., Suss, J.F., Fonseca, R.C.S., Alkmim, F.F., 2017a. Ediacaran forebulge grabens of the southern São Francisco basin, SE Brazil: craton interior dynamics during West Gondwana assembly. *Precambrian Res.* 302, 150–170.
- Reis, H.L.S., Alkmim, F.F., Fonseca, R.C.S., Nascimento, T.C., Suss, J.F., Prevatti, L.D., 2017b. The São Francisco basin. In: Heilbron, M., Cordani, U.G., Alkmim, F.F. (Eds.), *São Francisco Craton, Eastern Brazil, Regional Geology Reviews*. Springer, Switzerland, pp. 117–143.
- Rossi, A.V.A., Danderfer Filho, A., Bersan, S.M., Kelmer, L.R., Tavares, T.D., Lana, C.C., 2020. Stratigraphic, isotopic, and geochronological record of a superposed proforeland basin in the eastern São Francisco craton during west Gondwana amalgamation. *J. S. Am. Earth Sci.* 97, 102406.
- Sanchez, E.A.M., 2014. Microbialitos e microfósseis da Formação Sete Lagoas, Neoproterozoico, Brasil: implicações geomicrobiológicas em um contexto de mudanças climáticas e evolutivas. Universidade de São Paulo, p. 298. Ph.D. Dissertation.
- Sanchez, E.A.M., Vieira, T.A., Reis, H.L.S., Kuchenbecker, M.H., 2018. Microbialitos fósseis da Formação Jaíba, Grupo Bambuí, Minas Gerais, Brasil. *Rev. Bras. Palaontol.* 21 (2), 175–186.
- Sanchez, E.A.M., Uhlein, A., Fairchild, T.R., 2021. *Treptichnus Pedum* in the Três Marias Formation, south-central Brazil, and its implications for the ediacaran-cambrian transition in south America. *J. S. Am. Earth Sci.* 105, 102983.
- Sansjofre, P., Trindade, R.I.F., Ader, M., Soares, J.L., Nogueira, A.C.R., Tribouillard, N., 2014. Paleoenvironmental reconstruction of the Ediacaran Araras platform (Western Brazil) from the sedimentary and trace metals record. *Precambrian Res.* 241, 185–202.
- Santos, R.V., Alvarenga, C.J.S., Dardenne, M.A., Sial, A.N., Ferreira, V.P., 2000. Carbon and oxygen isotope profiles across meso-neoproterozoic limestones from central Brazil: bambuí and paranoá groups. *Precambrian Res.* 104, 107–122.
- Scott, C., Lyons, T.W., 2012. Contrasting molybdenum cycling and isotopic properties in euxinic versus non-euxinic sediments and sedimentary rocks: refining the paleoproxies. *Chem. Geol.* 324, 19–27.
- Shen, Y., Zhao, R., Chu, X., Lei, J., 1998. The carbon and sulfur isotope signatures in the Precambrian-Cambrian transition series of the Yangtze Platform. *Precambrian Res.* 89, 77–86.
- Spangenberg, J.E., Bagnoud-Velásquez, M., Boggiani, P.C., Gaucher, C., 2013. Redox variations and bioproductivity in the Ediacaran: evidence from inorganic and organic geochemistry of the Corumbá Group, Brazil. *Gondwana Res.* 26 (3), 1186–1207.
- Sweere, T., van den Boorn, S., Dickson, A.J., Reichart, G.J., 2016. Definition of new trace-metal proxies for the controls on organic matter enrichment in marine sediments based on Mn, Co, Mo and Cd concentrations. *Chem. Geol.* 441, 235–245.
- Tavares, T.D., Martins, M.S., Alkmim, F.F., Lana, C., 2020. Detrital zircons from the upper Três Marias Formation, São Francisco Basin, SE Brazil: record of foreland deposition during the cambrian? *J. S. Am. Earth Sci.* 97, 102395.
- Taylor, S.R., McLennan, S.M., 1985. *The Continental Crust: its Composition and Evolution*. Blackwell, Oxford, p. 312.
- Tribouillard, N., Algeo, T.J., Lyons, T., Riboulleau, A., 2006. Trace metals as paleoredox and paleoproductivity proxies: an update. *Chem. Geol.* 232, 12–32.
- Tribouillard, N., Algeo, T.J., Baudin, F., Riboulleau, A., 2012. Analysis of marine environmental conditions based on molybdenum–uranium covariation—applications to Mesozoic paleoceanography. *Chem. Geol.* 324–325, 46–58.
- Turekian, K.K., Wedepohl, K.H., 1961. Distribution of the elements in some major units of the Earth's crust. *Geol. Soc. Am. Bull.* 72, 175–192.
- Uhlein, A., Baptista, M.C., Seer, H.J., Caxito, F.A., Uhlein, G.J., Dardenne, M.A., 2011. A Formação Lagoa Formosa, Grupo Bambuí (MG): sistema deposicional de leque submarino em bacia de antepaís. *Geonomos* 19 (2), 163–172.
- Uhlein, G.J., Uhlein, A., Stevenson, R., Halverson, G.P., Caxito, F.A., Cox, G.M., 2017. Early to late Ediacaran conglomeratic wedges from a complete foreland basin cycle in the southwest São Francisco Craton, Bambuí Group, Brazil. *Precambrian Res.* 299, 101–116.
- Uhlein, G.J., Uhlein, A., Pereira, E., Caxito, F.A., Okubo, J., Warren, L.V., Sial, A.N., 2019. Ediacaran paleoenvironmental changes recorded in the mixed carbonate siliciclastic Bambuí Basin, Brazil. *Palaeogeogr. Palaeoclimatol. Palaeoecol.* 517, 39–51.
- Usma, C., Sial, A.N., Ferreira, V.P., Gaucher, C., Frei, R., 2021. Ediacaran banded iron formations and carbonates of the Cachoeirinha Group of NE Brazil: paleoenvironmental and paleoredox conditions. *J. S. Am. Earth Sci.* 109, 103282.
- Valeriano, C.M., 2017. The southern Brasília belt. In: Heilbron, M., Cordani, U.G., Alkmim, F.F. (Eds.), *São Francisco Craton, Eastern Brazil: Tectonic Genealogy of a Miniature Continent*. Springer, Switzerland, pp. 189–204.
- Vieira, L.C., Trindade, R.I.F., Nogueira, A.C.R., Ader, M., 2007b. Identification of a sturtian cap carbonate in the neoproterozoic Sete Lagoas carbonate platform, Bambuí Group, Brazil. *Compt. Rendus Geosci* 339, 240–258.
- Warren, L.V., Quaglio, F., Riccomini, C., Simões, M.G., Poiré, D.G., Strikis, N.M., Anelli, L.E., Strikis, P.C., 2014. The puzzle assembled: Ediacaran guide fossil *Cloudina* reveals an old proto-Gondwana seaway. *Geology* 42 (5), 391–394.
- Yang, J., Lyons, T.W., Zeng, Z., Odiage, K.O., Bates, S., Hu, L., 2019. Geochemical constraints on the origin of neoproterozoic cap carbonate in the helan mountains, north China: implications for mid-late ediacaran glaciation? *Precambrian Res.* 331, 105361.
- Zheng, Y., Anderson, R.F., van Geen, A., Kuwabara, J.S., 2000. Authigenic molybdenum formation in marine sediments: a linkage to pore water sulfide in the Santa Barbara Basin. *Geochim. Cosmochim. Acta* 64, 4165–4178.